Applied Thermal Engineering 285 (2026) 129206

Contents lists available at ScienceDirect

Applied Thermal Engineering

journal homepage: www.elsevier.com/locate/apthermeng

Research Paper

Experimental investigation on heat transfer to supercritical CO_2 in a microtube up to 30 MPa for application in the NET Power cycle

Iván Velázquez [a,*], Danilo A. Cantero [b], Frederiek Demeyer [c], Miriam Reyes [a]

[a] Department of Energy and Fluid Mechanics Engineering, University of Valladolid, Paseo del Cauce 59, 47011 Valladolid, Spain
[b] The Institute of Bioeconomy, PressTech, Department of Chemical Engineering and Environmental Technology, University of Valladolid, Paseo Prado de la Magdalena 5, 47011 Valladolid, Spain
[c] Department of Mechanics & Thermal Processes, Engie R&I (Laborelec), Rodestraat 125, 1630 Linkebeek, Belgium

ARTICLE INFO

Keywords:
NET power cycle
Oxy-combustion
Compact heat exchangers
Neural network
Heat transfer
Supercritical carbon dioxide
Microtube heat exchanger

ABSTRACT

Microtube heat exchangers represent a high-performance alternative to conventional printed circuit designs for the thermal recuperator of the innovative oxy-combustion NET Power cycle, offering potential improvements in both system efficiency and compactness. To support this technology transition, this study presents an experimental investigation of heat transfer in CO_2 at supercritical pressures up to 30 MPa. Experiments were conducted using a 1700 mm long, 0.88 mm inner diameter, uniformly heated horizontal microtube designed to replicate the operating conditions of a microtube heat exchanger. An experimental setup was built to measure local heat transfer coefficients of CO_2, with a parametric analysis performed to evaluate the influence of mass flux, heat flux, inlet temperature, buoyancy, and flow acceleration. Tests were conducted at pressures of 10, 15, 20, 25 and 30 MPa. Results show that the heat transfer improves with increasing mass flux. At 10 MPa, the heat transfer coefficient exhibits a peak near the pseudo-critical temperature, followed by a deterioration and subsequent recovery. With increasing thermal input, the peak is attenuated, while heat transfer performance improves at higher pressures. Raising inlet temperatures enhances heat transfer in the thermal inflow region, reduces the peak value at 10 MPa, and causes the heat transfer coefficients to converge across different pressures. Buoyancy effects are most pronounced at 10 MPa and become weaker as pressure increases. Moreover, a new deep neural network model was developed to predict heat transfer coefficients, demonstrating an average deviation of 6.34 %. The present study substantially expands the existing experimental database, provides new physical interpretations of key phenomena, and translates these findings into a predictive tool applicable to engineering design.

1. Introduction

The NET Power cycle is a highly-recuperative, high-pressure ratio, semi-closed power cycle for zero-emission energy production. It achieves an efficiency of 55.94 % [1], and a total specific cost of 1560 € kW^{-1} [2–4]. A schematic of the cycle is presented in Fig. 1. The cycle is based on an oxy-combustion process of natural gas and pure oxygen in a supercritical CO_2 ($scCO_2$) environment [5]. After expansion, the resulting flue gases, primarily CO_2 (93 % mol), H_2O (6 % mol) and trace impurities, are cooled below the dew point in a recuperative heat exchanger (RHE). Then, the gas mixture is compressed and further cooled to reach a supercritical liquid-like state at 8 MPa and 25 °C [6], characterized by liquid-like densities ($\rho \sim 10^3$ kg m^{-3}) and gas-like viscosities ($\mu \sim 10^{-5}$ Pa s). The supercritical fluid is then compressed to about 30 MPa, preheated in the RHE, and recirculated to the oxy-combustor to complete the cycle. The liquid-like behavior of CO_2 under supercritical regime significantly reduces compression work, thereby enhancing the overall cycle efficiency.

To obtain the $scCO_2$ at liquid-like conditions, the recycled CO_2 must be cooled in the RHE from about 765 °C (turbine exhaust) [1] to near the critical temperature (~31 °C). This results in an extremely high heat flux within the RHE. Additionally, a 5 °C pinch-point is specified [7] to maximize thermal effectiveness. Under these demanding conditions, conventional heat exchangers would require impractically large exchange areas. As an alternative, compact heat exchangers (CHE) have emerged as a viable solution [8]. CHEs are based on reducing the hydraulic diameter of flow channels to the microscale ($D_h \sim$ 1–1000 μm),

* Corresponding author.
E-mail address: ivan.velazquez@uva.es (I. Velázquez).

https://doi.org/10.1016/j.applthermaleng.2025.129206
Received 10 September 2025; Received in revised form 18 November 2025; Accepted 19 November 2025
Available online 22 November 2025

Nomenclature

b	bias
c_p	specific heat at constant pressure, kJ kg^{-1} K^{-1}
D	diameter, m
D_h	hydraulic diameter, m
f	friction factor
G	mass flux, kg m^{-2} s^{-1}
g	gravitational acceleration, m s^{-2}
Gr	Grashof number
h	specific enthalpy, kJ kg^{-1}
I	intensity of current, A
Ja	Jackson parameter for buoyancy
K_v	McEligot parameter for flow acceleration
L	length, m
M	number of layers of the neural network
$\dot{m}$	mass flow rate, kg s^{-1}
N	number of testing points
Nu	Nusselt number
p	pressure, MPa
p_r	reduced pressure; (p/p_{cr})
Pr	Prandtl number
$\dot{q}$	volumetric heat generation rate, W m^{-3}
$\dot{q}_w$	heat flux, kW m^{-2}
r	radial coordinate, m
Re	Reynolds number
Ri	Richardson number
T	temperature, °C
U	voltage, V
w	synaptic weight
x	axial distance, m
$\boldsymbol{x}$	vector of inputs to the heat transfer model

Greek symbols

α	heat transfer coefficient, kW m^{-2} K^{-1}
β	volumetric expansivity, K^{-1}
η	thermal efficiency of the test section
λ	thermal conductivity, W m^{-1} K^{-1}
μ	dynamic viscosity, Pa s
ν	kinematic viscosity, m^2 s^{-1}
ξ_{ac}	coefficient of acceleration resistance
ξ_{Pe}	coefficient of friction resistance
ρ	density, kg m^{-3}
σ	experimental uncertainty
ψ	Jackson parameter for flow acceleration

Subscripts

ave	average
b	bulk
calc	calculated
cr	critical
exp	experimental
f	film
h	heated
i	inner
in	inlet
o	outer
pc	pseudo-critical
th	threshold
w	wall

Superscripts

–	mean
+	dimensionless

Acronyms

CHE	compact heat exchanger
DC	direct current
DNN	deep neural network
HU	hidden unit
MAPE	mean average percentage error
MSTE	micro shell-and-tube exchanger
PCHE	printed circuit heat exchanger
RHE	recuperative heat exchanger
scCO$_2$	supercritical CO$_2$

thereby increasing the heat exchange area per unit volume [9]. In the context of the NET Power cycle, CHEs are particularly advantageous, as they can exploit the liquid-like behavior of scCO$_2$ to induce micro-confined turbulence, overcoming the traditional limitation of CHEs to operate within the laminar flow regime [10].

The dominant CHE design for the NET Power cycle is the printed circuit heat exchanger (PCHE). PCHEs are composed of flat metal plates with chemically-etched zig-zag flow channels, akin to printed circuit board fabrication [11]. These plates are alternately stacked and diffusion bonded to form a compact heat transfer block [12]. The NET Power cycle demonstration plant in LaPorte, Texas, employs PCHEs with 1.6 mm etched plates for its RHE units [7]. On the other hand, the micro shell-and-tube exchanger (MSTE) has gained interest for its advantages over PCHEs. MSTEs are miniaturized versions of conventional shell-and-

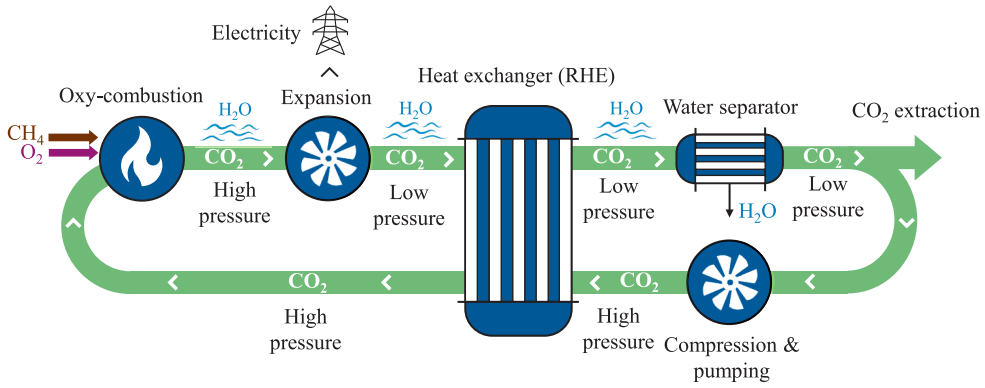

Fig. 1. Schematic representation of the oxy-combustion-based NET Power cycle.

tube heat exchangers, containing up to 80,000 microtubes [13,14]. They benefit from a well-established manufacturing supply chain, unlike the complex etching and diffusion techniques required for PCHEs. MSTEs also offer higher surface area density (4500 m^2 m^{-3} vs. 2500 m^2 m^{-3}) [8], enabling more efficient heat transfer with reduced material use, faster transients, and lower fabrication costs [15]. The former is important for the high-temperature sections using costly nickel-based superalloys [16]. Additionally, MSTEs outperform PCHEs in cleanability and maintenance. Exposure to $scCO_2$ causes significant oxidation [17], requiring regular maintenance to avoid clogging. While PCHEs are not serviceable without destroying the core, MSTEs can be easily accessed by removing the outer flange.

This work initiates research on heat transfer in $scCO_2$ under the theoretical scenario of a MSTE operating in the NET Power cycle RHE. On this basis, it should be noted that the recirculating $scCO_2$ stream is heated across the pseudo-critical region [18], where fluid properties exhibit rapid non-linear variations with a change in temperature [19], as illustrated in Fig. 2. The temperature at which the specific heat (c_p) peaks for a given pressure is referred to us as the pseudo-critical temperature (T_{pc}). The density varies significantly in the pseudo-critical domain. At temperatures below T_{pc}, the fluid presents a liquid-like behavior and above T_{pc} a gas-like behavior, resulting in a phase change from liquid- to gas-like properties without phases coexistence [20]. As pressure increases, T_{pc} increases and the properties change becomes smoother.

A turbulent flow in a horizontally-oriented heated straight tube experiences an enhancement of heat transfer in the vicinity of the pseudo-critical point by virtue of the steep increase in the Prandtl number (Fig. 2 (b)) [21]. The exact magnitude of this enhancement is influenced by axial and radial density gradients [22]. Axial density gradients cause a flow acceleration effect to satisfy the continuity of mass, which can potentially laminate the turbulent boundary layer. Radial density gradients generate buoyancy-induced secondary cross-flows that enhance turbulent fluid mixing and improve heat transfer rates [23,24].

Table 1 shows the experimental studies on heat transfer in $scCO_2$, flowing through horizontal tubes, that have been conducted. Adebiyi et al. [25] used a large horizontal tube with an inner diameter of 22.14 mm, and an inlet Reynolds number range of about $2\bullet10^4$–$2\bullet10^5$. The results revealed that the wall temperature at the top surface of the tube is higher than at the bottom surface because of the buoyancy-induced secondary cross-flow. This demonstrates an enhancement of heat transfer at the bottom of the tube and a deterioration at the top. Theologou et al. [26] experimentally examined the influence of Reynolds number and heat-to-mass flux ratio on thermal stratification in heated horizontal tubes of 4 mm and 8 mm. The heat-to-mass ratios were set between 38 and 225 J kg^{-1}. Increasing Reynolds numbers, for a given heat flux and tube diameter, reduces the temperature difference between the top and bottom of the tube. Increasing the tube diameter and the heat-to-mass flux ratio produces a more pronounced thermal stratification [23].

Research on $scCO_2$ heat transfer was recently focused on microchannels, as the work performed by Jajja et al. [35], in which they determined whether heat transfer mechanisms in large horizontal tubes can be extrapolated to the microscale. Experiments with 0.75 mm flow channels, under non-uniform heat flow conditions, were conducted. Authors concluded that buoyancy forces and flow acceleration are significant enough to influence the heat transfer process at the microscale. Wang et al. [37] experimentally investigated the heat transfer characteristics in horizontal tubes of diameter 1.0 mm, 0.75 mm and 0.5 mm. The heat transfer coefficients improved near the pseudo-critical point, finding that the configuration with higher mass flux, lower inlet temperature and smaller diameter exhibited the best heat transfer performance. In addition, authors concluded that the buoyancy effect may be insignificant for hydraulic diameters equal or smaller than 0.75 mm, although it was substantial for the 1 mm flow channel. Öztabak et al. [38] experimentally investigated the heat transfer characteristics of $scCO_2$ flowing through a horizontal 0.509 mm inner diameter microtube. Test were conducted at a pressure of 8 MPa and low Reynolds numbers, ranging from 400 to 1000 at the tube inlet. An evaluation of the Richardson number, which quantifies the relative influence of natural convection versus forced convection, showed that buoyancy forces near the wall significantly influence the heat transfer process. An increase in wall heat flux results in a reduction of Nusselt number in the region near the pseudo-critical point.

Most existing experimental studies on heat transfer in $scCO_2$ focused on large-diameter channels and pressures close to the CO_2 critical point (see Table 1) [39]. However, these conditions deviate from those relevant to emerging MSTEs intended for the NET Power cycle, represented by microtubes with diameters below 1 mm and higher pressures, typically between 10 and 30 MPa. Despite its relevance, there is a lack of experimental data under these specific conditions, which limits the understanding and modeling of heat transfer in $scCO_2$ for such applications. To address this research gap, the present study conducts an experimental investigation of heat transfer in $scCO_2$ within the 10–30 MPa pressure range, using a uniformly heated, horizontally-oriented microtube of 0.88 mm inner diameter and 1700 mm length. The objective is twofold:

1. To analyze heat transfer performance based on key variables such as mass flux, heat flux, inlet temperature, buoyancy, and flow

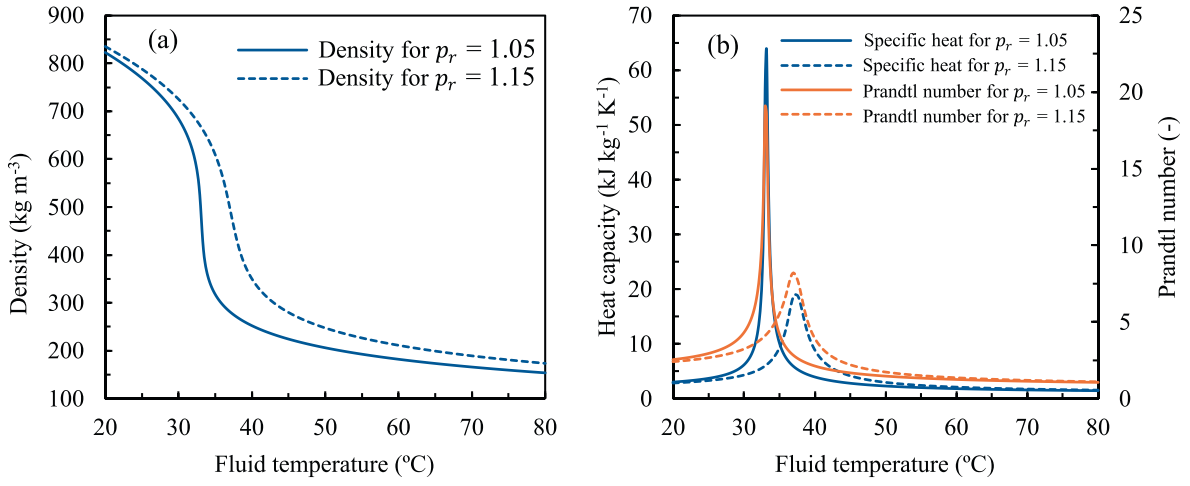

Fig. 2. Variation of the (a) density, (b) specific heat and Prandtl number as a function of the fluid temperature and reduced pressure (p_r) for pure CO_2.

Table 1
Experimental studies on heat transfer in $scCO_2$ flowing through horizontal tubes.

Authors	Tube diameter *ID* (mm)	Testing pressure *p* (bar)	Inlet temperature T_{in} (°C)	Mass flux *G* (kg m^{-2} s^{-1})	Heat flux $\dot{q}_w$ (kW m^{-2})	Method
Adebiyi et al. [25]	22.14	76	10.0–30.1	103.9–392.2	5.1–26.9	Heating
Liao et al. [27]	0.7, 1.4, 2.16	74–120	20	90.97–909.7	10–200	Heating
Yoon et al. [28]	7.73	75–88	50–80	225–450	–	Cooling
Dang et al. [29]	1–6	80, 90, 100	30–70	200–1200	6–33	Cooling
Huai et al. [30]	1.31	74–85	22–53	113.7–418.6	0.8–9	Cooling
Son et al. [31]	7.75	75–100	90–100	200–400	–	Cooling
Oh et al. [32]	4.55, 7.75	75–100	90–100	200–600	–	Cooling
Pita et al. [33]	4.72	77.9–134.2	91–126	1120.2–2211.8	40–70	Cooling
Liu et al. [34]	4, 6, 10.7	75–85	25–67	74.1–795.8	–	Cooling
Jajja et al. [35]	0.75	76–81.2	16–50	500–1000	200–400	Heating
Kim et al. [36]	7.75	73.8–77.4	24.5–30.1	52.1–250.5	1.2–25.9	Heating
Wang et al. [37]	0.5, 0.75, 1	76.6–90.0	31	848.8–3395.3	124.8–281.8	Heating
Theologou et al. [26]	4, 8	77.5	5–25	400, 800	30–130	Heating
Öztabak et al. [38]	0.509	80	27	79–141	6.4–9.3	Heating

acceleration, including their engineering implications in the design of MSTE units for the NET Power cycle.
2. To develop a deep learning-based heat transfer model from the generated data points that coherently integrates all major effects observed experimentally.

An overview of the experimental apparatus, data reduction, and test ranges are provided in Section 2. Results of the parametric study are discussed in Section 3. The novel heat transfer model is presented in Section 4. Finally, the main conclusions and findings are summarized in Section 5.

2. Experimental system and procedures

2.1. Experimental setup

An experimental rig was constructed to measure convective heat transfer coefficients of $scCO_2$ through a uniformly heated horizontal microtube. Although the recirculating CO_2 stream of the NET Power cycle contains traces of impurities, estimated at approximately 2 % mol [2], it was assumed that pure CO_2 models the actual flow with sufficient accuracy. Fig. 3 shows the schematic process diagram of the experimental apparatus. The main parameters measured and controlled are five: the testing pressure, mass flow, fluid temperature at the inlet and outlet of the test section, and the applied heat flux.

To obtain the fluid at supercritical conditions, CO_2 at a pressure of 45 – 70 bar, coming from a 99.5 % CO_2 purity cylinder, is cooled down to −2 °C in a heat exchanger which uses a mixture of ethylene–glycol and water at −12 °C as coolant (1 in Fig. 3). The liquified CO_2 is pressurized to the test pressure using a liquid pump (Milton Roy model MD 140 H6 M400), with a discharge pressure of up to 347 bar and a maximum volumetric flow of 4.17 L h^{-1} (2). A ball valve (4) allows flow through the experimental system.

The mass flow was varied by acting on the pump stroke. A Coriolis-type digital mass flow meter (3), with a nominal range of 0–25 kg h^{-1}, was used to measure the mass flow with a measurement uncertainty of ±1 %. The pressure of the CO_2 at the inlet of the test section was monitored by a pressure meter (Swagelok), with a range up to 400 bar. To adjust the fluid pressure at the inlet of the test section, a diaphragm back-pressure control valve (GO BP-66 series regulator), located downstream of the test section, with a range up to 689.5 bar, was used (9). A thermostatically controlled wire heater (8), coiled on the outer surface of the back-pressure valve inlet and outlet connection tubes, ensures that the fluid is heated sufficiently to prevent freezing during gas decompression.

The fluid temperature at each location of the test rig was measured by K-type thermocouples with 1 °C of uncertainty. The fluid temperature at the inlet of the test section is a major parameter for calculating the axial enthalpy profile of the $scCO_2$ along the flow path. Hence, the fluid supplied by the pump is preheated to the desired temperature, within

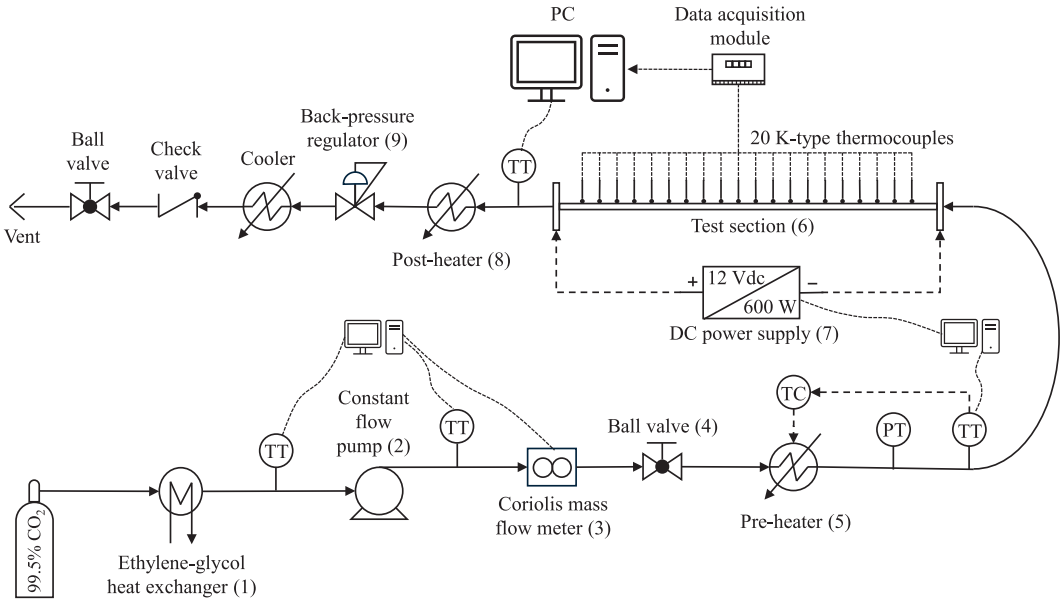

Fig. 3. Process flow diagram of the experimental system for the measurement of local heat transfer coefficients of $scCO_2$.

±0.2 °C, using a solid state relay-controlled wire heater, coiled on the outer surface of the tube (5).

To provide the required uniform heat flux, the test section (6) is heated through the passage of direct electric current (Joule effect), by applying voltage at the ends of the test tube with an adjustable DC power source (model bosytro 0–12 Vdc, 50 A, 600 W). A voltage and current meter measures (model ARCELI 200 A) the voltage and current in the test section with an uncertainty of 0.01 V and 0.01 A, and transmits data via serial port to the computer. Prior to venting, the fluid temperature is reduced in an air-cooled helical heat exchanger (10). A *virtual instrument* was developed in LabVIEW 2024 Q1 [40] to monitor and record real-time trends of the data captured by the sensors and control the test rig during experiments.

2.2. Test section design

A diagram of the test section is presented in Fig. 4. The test section consists of a 316L stainless steel circular microtube of length 1700 mm, and outer and inner diameters of 1.588 mm (1/16″) and 0.88 mm. The heated length was 1600 mm, with 100 mm of unheated hydraulic inflow length. The tube length was chosen in order to represent the actual tube length in MSTEs, which ranges between 1 and 3 m [13,14]. As shown in Fig. 4, a 3.175 mm (1/8″) helical-shaped stainless steel tube was placed at the end of the test section to gently pull the microtube and keep it straight, also allowing to absorb the stresses caused by the axial dilatation of the tubes during heating and to avoid leakages at fittings. The voltage on the heated section was applied using two copper clamps. The test section was electrically isolated from the rest of the experimental system to avoid interference with the measurement systems, using two Swagelok dielectric fittings (not shown in Fig. 4). Two PETG fasteners, manufactured by 3D printing, fix the dielectric fittings at the end of the test section to the aluminum frames, preventing electrical current shunts.

As was stated in the Introduction section, in horizontal flow configurations, the wall temperature may exhibit circumferential non-uniformity due to the buoyancy effects. However, the strength of buoyancy forces decreases significantly in miniature tubes, as it is proportional to the third power of the inner diameter ($F_{Bu} \propto D_i^3$). Furthermore, in this study, pressures of up to 30 MPa are reached, conditions under which density gradients decrease. Both effects lead to a reduction of the buoyancy forces and therefore essentially uniform wall temperature profiles. This trend was confirmed by dedicated CFD simulations reproducing the exact geometry of the test section, which showed negligible circumferential temperature differences for pressures between 15 and 30 MPa, and a maximum of 0.46 K for 10 MPa, near the pseudo-critical point. Therefore, only the temperature measurement on the top wall of the test tube was considered.

To measure the local outer wall temperature throughout the test section, 20 K-type sheathed thermocouples (0.5 mm diameter, ungrounded junction) were uniformly distributed at 76.2 mm intervals along the top surface of the tube. For attachment, the last 7 mm of the sheath were aligned longitudinally with the tube axis. The thermocouple tip, where the sensing junction is located, was held in direct contact with the surface using a polyester knot to ensure a stable mechanical assembly. The remaining final section of the aligned sheath was affixed to the tube by applying a thin layer of thermally-conductive epoxy adhesive (MG Chemicals 8329TTF), ensuring proper axial alignment of the sensing junction with the tube surface. Then, the entire aligned length was further secured with a Kapton tape to reinforce its fixation. The surface-mounted thermocouples presented an uncertainty of 0.5 °C after the application of the calibration function, provided by the manufacturer, in the surface temperature range covered in this work (up to 200 °C). Three I-7018 8-channel thermocouple input modules collect signals from the thermocouples. A tM-7561 module converts RS-485 to serial to establish communication with LabVIEW.

The test section was thermally insulated. To this end, the microtube was firstly encased by a 10 mm diameter high thermal resistance silicone tube, and an 80 mm diameter elastomeric foam outer layer. The outer insultation layer was thickened until the temperature of the outer surface, captured by a thermographic camera, was no higher than the ambient temperature when the test section was heated at a temperature of 150 °C.

2.3. Data reduction

Heat transfer in supercritical fluids is a local phenomenon due to the variation of the fluid properties. Hence, the data reduction analysis was based on local properties. For simplification in notation, the subscript x, which usually refers to the local property, was omitted. The testing tube was heated by direct electrical heating, assuming that the volumetric heat generation rate is uniform,

$$\dot{q} = \frac{UI}{\frac{\pi}{4}\left(D_o^2 - D_i^2\right)L_h}, \tag{1}$$

where U is the voltage, I is the intensity of current and L_h is the heated length. The outer wall of the testing tube is insulated. However, heat losses due to conduction through the surface-mounted thermocouples occur. To account for these losses, an efficiency parameter, η, was defined as follows:

$$\eta = \frac{\dot{m}\left(h_{b,out} - h_{b,in}\right)}{UI}. \tag{2}$$

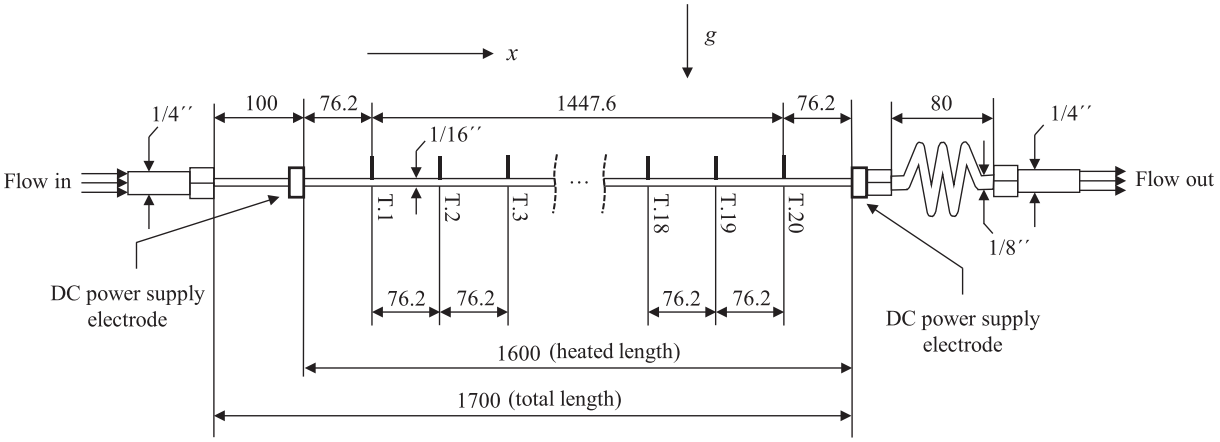

Fig. 4. Distribution of thermocouples along the outer wall of the test section. Units: mm, unless otherwise indicated.

In each experiment η was determined, with values ranging from 0.93 to 0.98. Lower η values were registered in tests conducted under higher heat fluxes and lower fluid superficial velocities. Therefore, the effective heat flux imposed on the inner wall of the tube is calculated as:

$$\dot{q}_w = \frac{\eta UI}{\pi D_i L_h}. \tag{3}$$

The axial distribution of mean enthalpy through the flow path can be determined based on the convective heat balance equation:

$$h_{b,x} = h_{b,x-\Delta x} + \frac{\pi D_i \dot{q}_w}{\dot{m}} \Delta x, \tag{4}$$

where Δx is the distance between two thermocouple locations. From the mean enthalpy and inlet fluid pressure (p_{in}), the corresponding bulk mean temperature is calculated using the NIST REFPROP software [41], i.e., $T_b = T_b(h_b, p_{in})$. The pressure drop was neglected in the data reduction, since the pressure drop values, presented in Appendix D of the supplementary materials, are sufficiently low to have no significant influence on the derivation of the heat transfer coefficients. For instance, in test T28, with a pressure drop of 0.52 bar, the maximum deviation in the heat transfer coefficient due to pressure drop is <0.4 %. Moreover, the pressure profile along the test section cannot be accurately determined using the experimental setup.

The temperature at the inner wall of the tube can be calculated from the outer wall temperature, measured by the thermocouples, based on the one-dimensional heat conduction equation (Eq. (5)), and the boundary conditions of the experiments (Eq. (6)):

$$\frac{1}{r}\frac{d}{dr}\left(r\frac{dT}{dr}\right) + \frac{\dot{q}}{\lambda} = 0 \tag{5}$$

$$\begin{aligned} &\text{i.} \lambda \left.\frac{dT}{dr}\right|_{r=r_o} = 0, \\ &\text{ii.} T(r_o) = T_{wo}. \end{aligned} \tag{6}$$

Integrating Eq. (5), the inner wall temperature was derived analytically as follows:

$$T_{wi} = T_{wo} + \frac{\dot{q}}{16\lambda}\left(D_o^2 - D_i^2\right) - \frac{\dot{q} D_o^2}{8\lambda} \ln\frac{D_o}{D_i}. \tag{7}$$

The heat transfer coefficient was obtained based on the Newton's cooling law:

$$\alpha = \frac{\dot{q}_w}{T_{wi} - T_b} \tag{8}$$

2.4. Uncertainty analysis

An analysis of the experimental uncertainties was performed based on the uncertainties of the measurement devices and the McClintock method [42]. The experimental uncertainty of the heat transfer coefficient was calculated using Eq. (9).

$$\frac{\sigma_\alpha}{\alpha} = \sqrt{\left(\frac{\sigma_{\dot{q}_w}}{\dot{q}_w}\right)^2 + \left(\frac{\sigma_{T_{wi}}}{T_{wi} - T_b}\right)^2 + \left(\frac{\sigma_{T_b}}{T_{wi} - T_b}\right)^2} \tag{9}$$

The uncertainties of the wall heat flux $\sigma_{\dot{q}_w}$ (Eq. (10)), inner wall temperature $\sigma_{T_{wi}}$ (Eq. (11)), and bulk mean temperature σ_{T_b} (Eq. (12)), were derived from Eqs. (3), (7) and (4), respectively.

$$\frac{\sigma_{\dot{q}_w}}{\dot{q}_w} = \sqrt{\left(\frac{\sigma_U}{U}\right)^2 + \left(\frac{\sigma_I}{I}\right)^2} \tag{10}$$

$$\sigma_{T_{wi}} = \sqrt{(\sigma_{T_{wo}})^2 + \left[\left(\frac{D_o^2 - D_i^2}{16\lambda} - \frac{D_o^2}{8\lambda}\ln\frac{D_o}{D_i}\right)\sigma_{\dot{q}}\right]^2} \tag{11}$$

$$\sigma_{h_{b,x}} = \sqrt{\left(\sigma_{h_{b,x-\Delta x}}\right)^2 + \left(\frac{\pi D_i \Delta x}{\dot{m}}\sigma_{\dot{q}_w}\right)^2 + \left(\frac{\pi D_i \Delta x \dot{q}_w}{\dot{m}^2}\sigma_{\dot{m}}\right)^2} \tag{12}$$

The measurement uncertainties of the voltage σ_U, electric current σ_I, mass flow rate $\sigma_{\dot{m}}$ and outer wall temperature $\sigma_{T_{w,o}}$ are 0.1 %, 0.1 %, 0.5 % and 0.5 °C, respectively.

2.5. Experimental ranges and test conditions

The main experimental variables influencing the heat transfer mechanisms of $scCO_2$ are the pressure, mass flux, heat flux and fluid temperature at the inlet of the test tube. In this work, the experimental design conducted in the software Statgraphics Centurion 19 [43], which is based on the fractional factorial model, covers the operational region of the low temperature heat exchanger of the NET Power cycle with a reduced number of tests and without compromising statistical reliability, evaluating the influence of these experimental variables on the heat transfer coefficients.

The experimental ranges of pressure, bulk enthalpy and bulk temperature are shown in Fig. 5 within the blue domain. The blue dots represent the specific conditions where the heat transfer coefficients were acquired. The exact experimental conditions of each test are given in Appendix A of the supplementary materials. The pressure of the $scCO_2$ within the RHE of the NET Power cycle ranges between approximately 10 and 30 MPa, depending on the cycle load degree [44]. Therefore, tests were conducted for five equally distributed pressures, i.e.: 10, 15, 20, 25 and 30 MPa. The inlet temperature of the $scCO_2$ in the NET Power cycle RHE ranges between 25 and 45 °C, depending on the load degree. Hence, the experiments were performed for two fluid inlet temperatures, 20 ± 0.2 °C and 30 ± 0.2 °C. Then, heat transfer coefficients up to 45 °C are measured along the tube length. The Reynolds number ranged between 4100 and 23847, which is in agreement with a maximum flow velocity through the tube of about 2–2.5 m s^{-1} in industrial-scale MSTEs [13,14,45].

The maximum test fluid temperature was assumed to be 100 °C. Above this temperature, the fluid collapses to a constant-property single supercritical gas-like phase [24]. In Fig. 5, the red region represents the experimental domain covered in the previous studies, listed in Table 1. The experimental extension highlights the novelty of this study. The proposed design of experiments resulted in a total of 28 tests, which

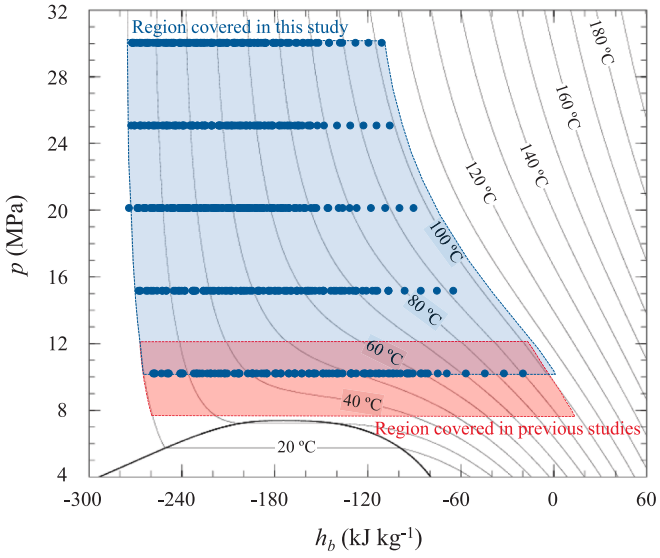

Fig. 5. Experimental pressure and bulk enthalpy (or bulk temperature) ranges explored in this study are represented by the blue domain, while those covered in previous studies (Table 1) are shown in the red domain.

cover the entire thermodynamic ranges.

2.6. Experimental procedure

A diagram of the experimental procedure is illustrated in Fig. 6. At start-up, the CO_2 and refrigerant inlet valves are opened to pressurize the system, keeping the vent valve close for leaks detection. After this verification, the vent is opened and the test tube and back-pressure valve are preheated using the DC power source and the post-heater.

Afterwards, the pump is turned on and the experimental parameters (pressure, mass flux, heat flux, and inlet temperature) are adjusted through the back-pressure regulator, pump stroke, voltage of the DC source, and pre-heater. The system is considered to have reached steady-state when the temperature variations of the fluid and the tube surface are <0.2 °C; the experiments begin 5 min after these conditions are reached. The data are recorded at a 10-minute interval with a frequency of 0.5 Hz.

After the test, the heat sources and pump are turned off, the inlet valves are closed, and the pressure in the system is released by opening the vent and back-pressure valves.

3. Heat transfer results and discussion

This first section of results presents the outcomes derived from the parametric study, which considers the effect of mass flux ($447.4 \leq G \leq 1044.5$ kg m^{-2} s^{-1}), heat flux ($8.3 \leq \dot{q}_w \leq 21.3$ kW m^{-2}), inlet temperature ($19.8 \leq T_{in} \leq 30.1$ °C), buoyancy and thermal flow acceleration on the heat transfer performance of $scCO_2$, for the test pressures of 10, 15, 20, 25 and 30 MPa.

In total 28 experiments were conducted, and 560 data points were collected in combinations of these experimental variables. The resulting data points and uncertainties are reported in Appendix D of the supplementary materials. From the total amount of tests, 25 tests were selected to conduct the sensitivity analysis; while the remaining 3 tests, T21, T27 and T28, were used to fit an empirical heat transfer model. The maximum uncertainties of the resulting heat transfer coefficients are located in the inflow length, where the heat transfer coefficients are high during the thermal boundary layer development, and in the region near the pseudo-critical point, where a minimum change in temperature causes a significant change in the fluid properties. The maximum uncertainty recorded was 18.18 %, although for most of the experiments the maximum range of relative deviation of the heat transfer coefficient was below 6 %.

An experimental repeatability study was conducted to ensure the reliability of the test rig and to avoid the influence of unforeseen factors. To this end, the T4 test at 10 MPa and the T24 test at 30 MPa were repeated twice and the deviations in the measurements of the tube outer-wall temperatures were evaluated. Results are shown in Fig. 7. For the T4 test, the maximum deviation recorded was 6.8 % near the pseudo-critical conditions, while for the T24 test it was 3.6 % at the entry region. It is important to note that these deviations do not originate solely from the thermocouples uncertainty. Uncertainties in the measurement and control of mass flux, pressure, inlet temperature, and heat input also play a significant role. Furthermore, conditions near the pseudo-critical point and inflow length are particularly sensitive to such uncertainties. Hence, these findings suggest that the experimental data are consistent, validating the repeatability of the experimental apparatus.

3.1. Effect of mass flux

Using the mass flux as an independent parameter, Fig. 8 shows the distributions of inner-wall temperature (left graph) and local heat transfer coefficient (right graph) as a function of bulk enthalpy and inlet distance from the heating onset, respectively. The heat flux and fluid temperature at the inlet of the test section were kept constant for each test pressure. The results show that heat transfer improves consistently with increasing mass flux for all tested pressures. This enhancement is attributed to the increase in the Reynolds number, which promotes

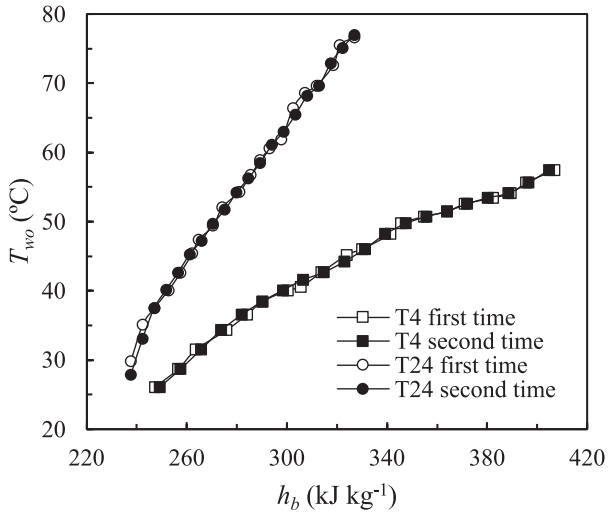

Fig. 7. Results of the repeatability analysis of the T4 and T24 tests. For T4 the maximum deviation is 6.8% near the pseudo-critical point, while for T24 it was 3.6% in the thermal inflow region.

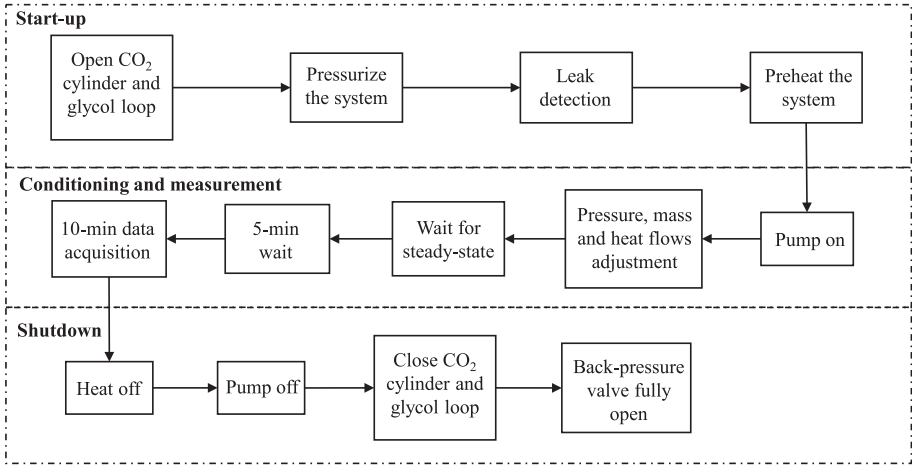

Fig. 6. Schematic representation of the experimental procedure.

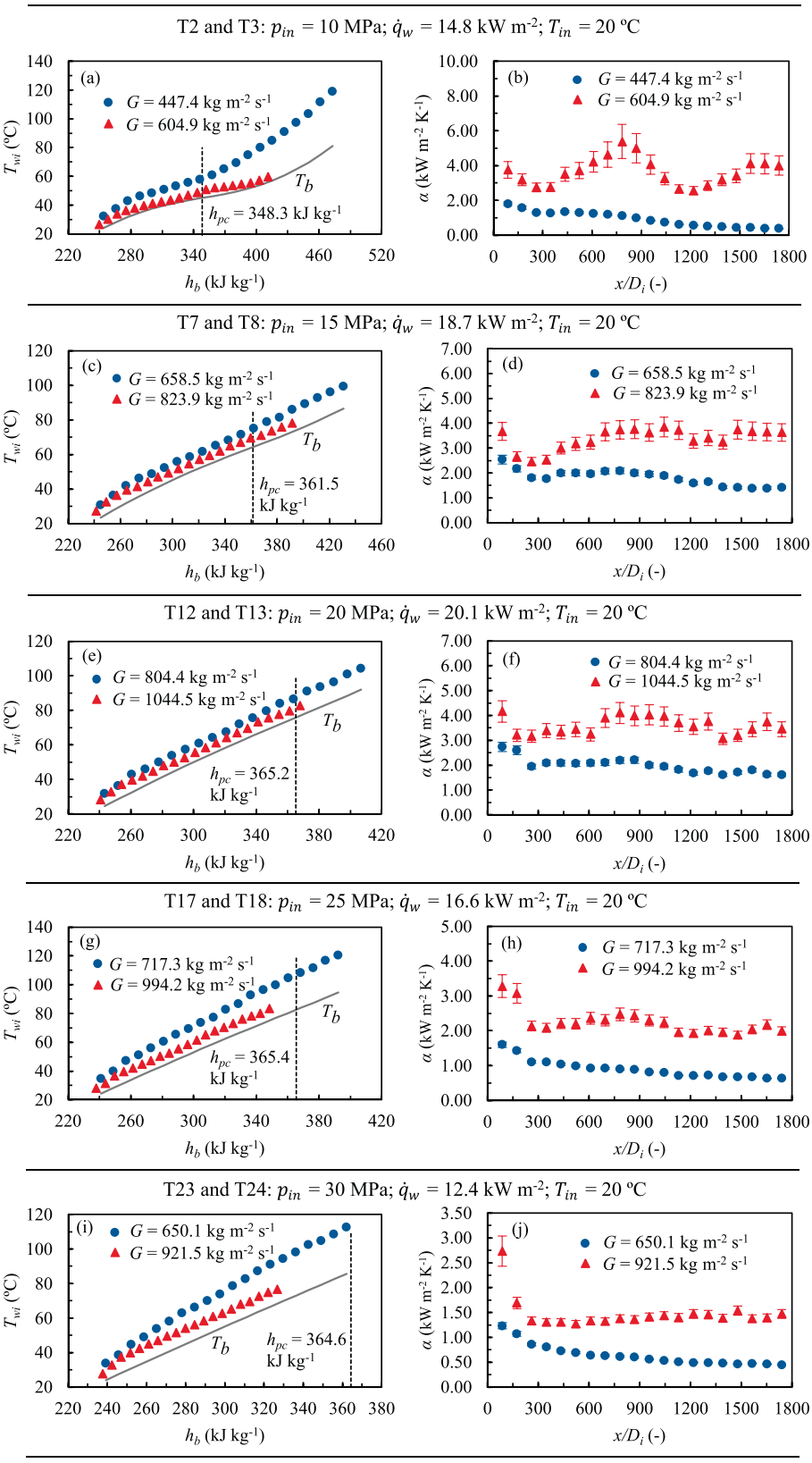

Fig. 8. Effect of mass flux on inner-wall temperature and local heat transfer coefficient for tests T2, T3, T7, T8, T12, T13, T17, T18, T23 and T24. The higher the mass flux, the higher the heat transfer coefficients.

stronger turbulent mixing and more efficient heat transport.

For 10 MPa and 604.9 kg m^{-2} s^{-1}, Fig. 8(b) shows that the heat transfer coefficient initially decreases along the thermal inflow length due to the gradual thickening of the thermal boundary layer. Thereafter, it increases as the bulk fluid temperature rises, reaching a peak value just before the pseudo-critical enthalpy. This peak is attributed to the rapid increase in the Prandtl number near the pseudo-critical point. As the bulk fluid temperature rises beyond the pseudo-critical temperature, the heat transfer coefficient declines, followed by a recovery to a constant value, forming a deteriorative valley region. Experimental studies conducted by Wang et al. [37] in miniature tubes were the first to report the formation of the deteriorative valley region. Therefore, this new data set confirms the appearance of a valley region around the pseudo-critical point in miniature tubes.

To give a physical explanation for the origin of the valley region, the phenomenon can be decomposed and examined independently in its two characteristic stages: the deterioration phase and the recovery phase. The heat transfer coefficient deterioration is due to buoyancy-induced secondary cross-flows, which accumulate low-momentum fluid in the upper part of the tube. This results in thermal stratification and a suppression of turbulent quantities. In contrast, the subsequent recovery of the heat transfer coefficient is driven by axial flow acceleration, which enhances the production of turbulent kinetic energy. Temperature stratification in the microtube leads to asymmetric thermal expansion between the top and bottom tube walls, potentially inducing thermal fatigue and promoting crack propagation issues.

When the mass flux was reduced to 447.4 kg m^{-2} s^{-1}, it was found that the valley region disappears and there is a monotonic decrease of the heat transfer coefficient after reaching the pseudo-critical point, as shown in Fig. 8(b). This trend has been reported in several previous studies involving large-diameter tubes [26,46–48]. The disappearance of the recovery zone within the valley region, observed for the first time in this study for microtubes at low mass flows, can be attributed to the reduction in axial flow acceleration with mass flux. This reduction limits the production of turbulent kinetic energy in the near-wall region induced by axial thermal expansion. Moreover, under constant heating power and inlet temperature, a reduction in mass flow leads to an increase in the fluid outlet temperature. As a result, the region downstream of the pseudo-critical enthalpy is extended, attenuating the heat transfer rates.

For 15, 20, 25 and 30 MPa, the peak values of the fluid properties near the pseudo-critical point are significantly lower than for 10 MPa. Therefore, as shown in Fig. 8(c–j), the trends of the heat transfer coefficient become flatter, with similarity to constant-property flows. For the lower values of mass flux used in the experiments, the heat transfer coefficients decrease smoothly along the flow path to a constant value, as deduced from the progressive separation of the inner-wall and bulk temperatures. This is a result of a larger thermal inflow length and a thick thermal boundary layer, which is a consequence of low Reynolds numbers. The higher the mass flux, the shorter the thermal inflow length.

3.2. Effect of heat flux

The effect of the heat flux in the evolution of the inner-wall temperature as a function of the bulk enthalpy (left graph), and the local heat transfer coefficient as a function of the bulk fluid temperature (right graph), are represented by Fig. 9. For this case, more meaningful insights were found by plotting the heat transfer coefficient as a function of bulk temperature rather than heating distance. For each test pressure, the mass flux and inlet temperature were maintained constant.

It can be seen in Fig. 9(b) that, when the pressure was fixed at 10 MPa, increasing the heat flux causes an attenuation of the heat transfer coefficient peak value, while the bulk fluid temperature at which peak occurs decreases. Increasing the heat flux causes an increase in the temperature difference between the near-wall and bulk fluid regions, intensifying the buoyancy effects, as deduced from the Grashof number definition (expressed in terms of $\dot{q}_w$) in Eq. (13).

$$Gr_q = \frac{g\bar{\beta}\dot{q}_w D_i^4}{\nu_b^2 \lambda_b} \tag{13}$$

$\bar{\beta}$ denotes the coefficient of volumetric expansivity $\bar{\beta} = (1/\rho_f) \bullet (\rho_b - \rho_w)/(T_w - T_b)$, with the density ρ_f evaluated at the film temperature $T_f = (T_w + T_b)/2$. Therefore, flow stratification is accentuated, with a significant suppression of the turbulent convection. In addition, Wang et al. [49] reported that, when buoyancy forces become sufficiently dominant, part of the low-density fluid, that ascends by natural circulation in the cross-section of the tube, counteracts the high-density flow descending along the centerline, mitigating the turbulent quantities. Both phenomena account for the reduction in the heat transfer coefficient peak. For bulk enthalpy values below the pseudo-critical point, the heat transfer coefficient tendency during thermal boundary layer development remains insensitive to variations in heat flux. However, for a constant mass flow and inlet temperature, increasing the heat flux rises the fluid outlet temperature and expands the enthalpy region beyond the pseudo-critical point, resulting in a reduction of heat transfer rates.

The enhancement of the $scCO_2$ heat transfer process at 10 MPa with the reduction of the heat flux is advantageous when considering the actual operating conditions of a MSTE within the NET Power cycle. Under minimum cycle load, the pressure of the recirculating $scCO_2$ flowing through the microtubes approaches 10 MPa, while the heat flux delivered by the exhaust gases decreases due to a mass flow reduction [44]. Thus, this finding reveals that the improvement of the heat transfer coefficient under these conditions helps to sustain high heat transfer effectiveness in the low-temperature section. This compensates for the diminished heat transfer rates caused by the mass flow reduction.

Fig. 9(c–j) show that, for pressures of 15, 20, 25 and 30 MPa, the heat transfer coefficients increase with rising thermal load. This finding is attributed to the reduction in fluid viscosity as temperature increases, which causes the Reynolds number to rise (under constant mass flux conditions). Consequently, as the thermal input increases, the average fluid temperature in the tube increases, resulting in higher average Reynolds numbers and enhanced turbulent diffusivity. This observation introduces a novel aspect with direct implications for MSTE design, as it reveals an enhancement of the thermal effectiveness of the MSTE under nominal conditions, when the heat flux reaches its maximum value.

3.3. Effect of inlet temperature

To clarify the effect of the fluid temperature at the inlet of the test tube, Fig. 10 depicts the trends of the inner-wall temperature and the local heat transfer coefficient as a function of the bulk fluid enthalpy and distance from the heated section, respectively. The mass flow and heat flux were kept constant for the five tested pressures. The inlet temperature adopted the values of 20 °C and 30 °C, within an accuracy of ±0.2 °C.

An increase in the fluid inlet temperature results in a higher heat transfer coefficient within the thermal inflow region. For a constant mass flow, the Reynolds number rises with the bulk fluid temperature due to the reduction in viscosity. Consequently, a higher inlet temperature leads to increased Reynolds numbers and greater turbulent intensity during the initial heating phase, enhancing heat transfer. However, beyond the inflow region, the heat transfer behavior exhibited qualitatively different trends depending on the tested pressure.

As depicted in Fig. 10(b) for 10 MPa, the heat transfer coefficient decreases with increasing inlet temperature. For a fixed mass flow and heat input, an elevated inlet temperature results in a higher fluid outlet temperature, which expands the gas-like enthalpy region beyond the pseudo-critical point, while reducing the liquid-like phase region below it. This leads to a deterioration in heat transfer performance. Notably,

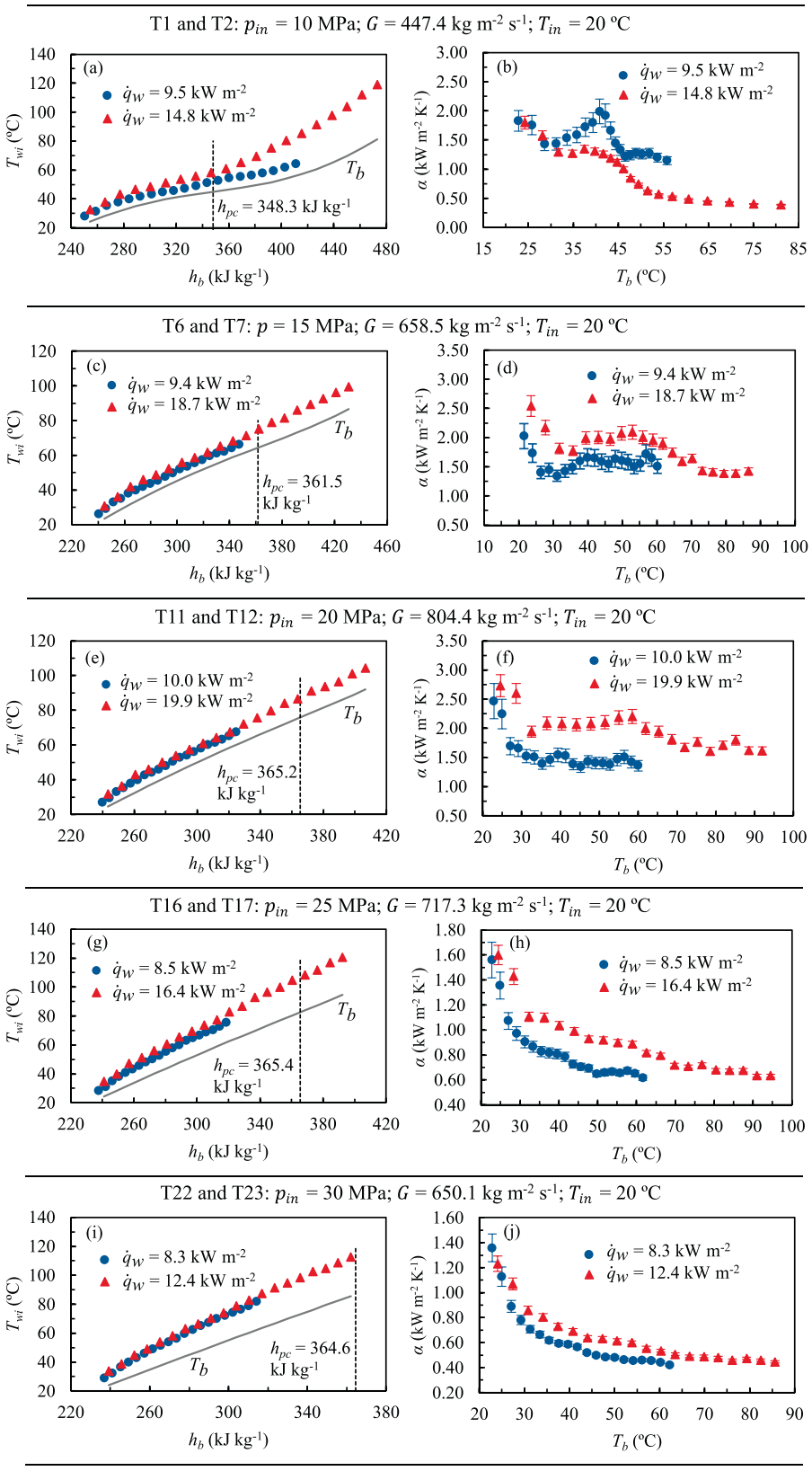

Fig. 9. Effect of heat flux on inner-wall temperature and local heat transfer coefficient for tests T1, T2, T6, T7, T11, T12, T16, T17, T22 and T23. At 10 MPa the heat transfer coefficients decrease with increasing heat flux, whereas at higher pressures they increase.

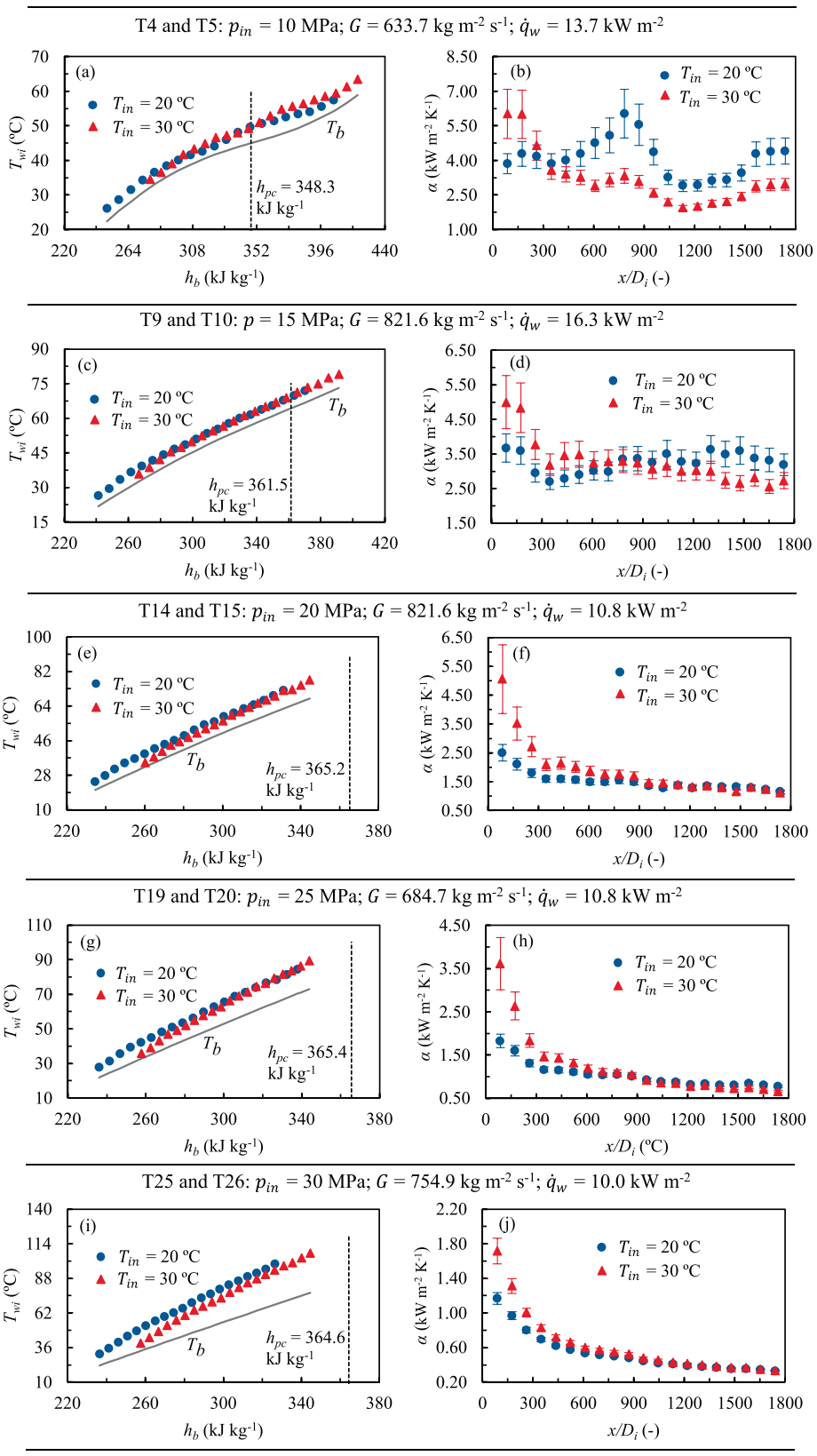

Fig. 10. Effect of inlet temperature on inner-wall temperature and local heat transfer coefficient for tests T4, T5, T9, T10, T14, T15, T19, T20, T25 and T26. The higher the fluid inlet temperature, the higher the heat transfer coefficients in the inlet region.

the bulk fluid temperature, corresponding to the peak heat transfer coefficient, remains insensitive to variations in inlet temperature. For the inlet temperatures examined (20 and 30 °C), a degradative valley region immediately follows the peak. Similar trends were reported in previous studies [26,37,48]. When the NET Power cycle operates at minimum load conditions, the inlet pressure and temperature of the $scCO_2$ flow are at minimum values. Hence, these findings reveal a heat transfer enhancement in the low-temperature section of the recuperative heat exchanger under such conditions.

For 15 MPa, Fig. 10(c) reveals an overlapping of the inner-wall temperatures after a certain length, indicative of a thermal fully developed flow [26]. However, for an inlet temperature of 30 °C, the widening of the pseudo-critical region, originated by the increase of the outlet temperature, leads to a slight reduction of the heat transfer coefficient near the end of the flow path, beyond the pseudo-critical point. This decline is less intense at 15 MPa than at 10 MPa. As shown in Fig. 10 (e–j), the local heat transfer coefficients exhibit a similar pattern as a function of the inlet temperature when the pressures were set at 20, 25 and 30 MPa. In the thermal inflow region, heat transfer is enhanced with increasing inlet temperature. Afterwards, the temperatures in the near-wall region overlap, leveling the heat transfer coefficients. Regarding the NET Power cycle working at nominal load, the $scCO_2$ pressure and temperature are at maximum values. Hence, this experimental study demonstrates that higher heat transfer rates may be expected within the thermal inflow region, slightly enhancing the overall effectiveness of the heat transfer process.

3.4. Effect of buoyancy

For turbulent mixed convection in horizontal flows, the best-known criterion to describe the influence of buoyancy on heat transfer is the Richardson number, *Ri* [50]. It has been previously applied by numerous authors to study supercritical fluid flows [23,26,27,37,51]. This criterion states that when natural convection has significant influence on the heat transfer,

$$Ri = \frac{Gr_b}{Re_b^2} > 10^{-3}. \tag{14}$$

The Grashof number Gr_b, that was defined in Eq. (13), relates the buoyancy and viscous forces. Other authors [26,35,52] have employed the criterion built by Petukhov and Polyakov [53], which proposes a threshold Grashof number Gr_{th}, defined in Eq. (15), that quantifies the strength of buoyancy forces.

$$Gr_{th} = 3 \bullet 10^{-5} \overline{Pr}^{0.5} Re_b^{2.75} \left[1 + 2.4 Re_b^{-1/8} \left(\overline{Pr}^{2/3} - 1\right)\right] \tag{15}$$

The Prandtl number $\overline{Pr}$ results from the integration of the specific heat to $\overline{Pr} = (\mu_b/\lambda_b) \bullet (h_w - h_b)/(T_w - T_b)$. Then, the Petukhov and Polyakov criterion states that when the effect of buoyancy-induced secondary flow does not significantly influence the heat transfer, the Gr_q/Gr_{th} ratio should be lower than the unity. Gr_q was previously defined in Eq. (13). Adebiyi et al. [25] and Tanimizu et al. [54] studied the criterion proposed by Jackson, which includes the thermal inflow length as an indication of the onset of buoyancy effects. The Jackson criterion establishes that in horizontal pipe flows, buoyancy effects cannot be neglected when

$$Ja = Ri \left(\frac{\rho_b}{\rho_w}\right) \left(\frac{x}{D_i}\right)^2 > 10. \tag{16}$$

Fig. 11 shows the buoyancy criterions of (a) Richardson, (b) Petukhov and (c) Jackson, plotted on a logarithmic scale, as a function of the distance from the heating onset, applied to the 560 experimental data points obtained in this work.

As shown in Fig. 11(a), the Richardson criterion states that, for 10 MPa, convective heat transfer is affected by buoyancy, especially in tube

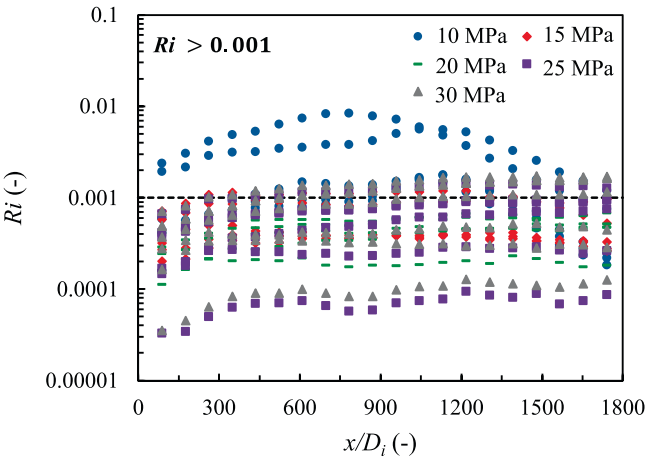

(a) Richardson criterion [50].

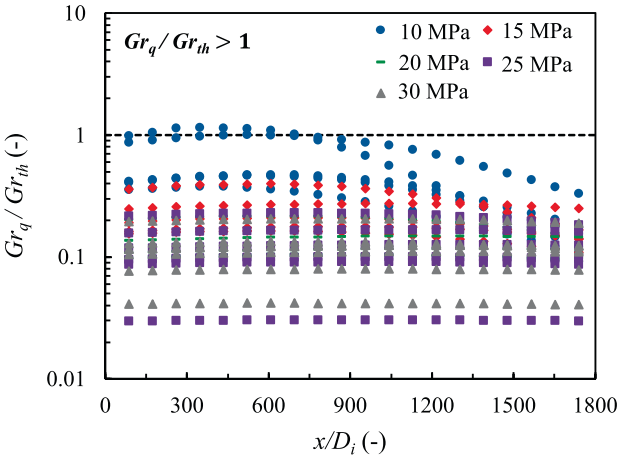

(b) Petukhov and Polyakov criterion [53].

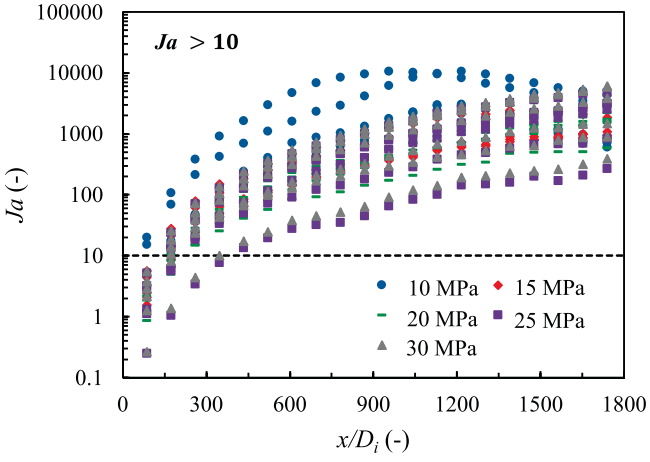

(c) Jackson criterion [25].

Fig. 11. (a) Richardson, (b) Petukhov and (c) Jackson criterions for buoyancy along the heated length as a function of the inlet pressure. Buoyancy significantly affects convective heat transfer at 10 MPa, but its influence decreases with increasing pressure, although mixed convection appears when the heat-to-mass flux ratio is high.

regions where the bulk enthalpy approaches the pseudo-critical enthalpy. For higher system pressures, the radial density gradients decrease, leading to a reduction in buoyancy effects. However, for experimental cases with a high $\dot{q}_w/G$ ratio, mixed convection is found for all tested pressures.

According to the Petukhov criterion, depicted in Fig. 11(b), only a few data points at 10 MPa are influenced by buoyancy. For pressures above 10 MPa, the Gr_q/Gr_{th} ratio remains below unity, indicating that buoyancy effects can be neglected. It can be seen in Fig. 11(b) that, for the tests conducted at 10 and 15 MPa, Gr_q/Gr_{th} increases along the tube to a peak before decreasing monotonically. This behavior results from the approximation of near-wall and bulk fluid temperatures in the vicinity of the pseudo-critical point, which causes a sharp increase in volumetric expansivity, and decrease in both kinematic viscosity and thermal conductivity. As the fluid is further heated beyond the pseudo-critical temperature, Gr_q/Gr_{th} decreases. The peak value of Gr_q/Gr_{th} increases with higher $\dot{q}_w/G$ values. For pressures above 15 MPa, the axial trend of Gr_q/Gr_{th} becomes flatter.

Fig. 11(c) shows that, for most experimental conditions and tested pressures, the Jackson parameter, *Ja*, is greater than 10, indicating the presence of mixed convection. Jackson introduces the thermal inflow length, so that values at the tube inlet depart from a low buoyancy influence and increase along the tube. The local *Ja* number for 10 MPa increases to a maximum value, which is close to 10,000, and then decreases. Similar tendencies were reported in previous studies [26]. For pressures above 10 MPa, all *Ja* values increase continuously throughout the tube. Moreover, Jackson criterion proves that the distance for which buoyancy effects start to become significant increases as the system pressure increases.

3.5. Effect of flow acceleration

Several criteria have been proposed to predict the potential heat transfer deterioration due to the thermally-induced flow acceleration effect. The criterion built by Jackson et al. [55], which defines the thermal acceleration parameter ψ as follows:

$$\psi = 10^4 \left(\frac{\beta_b \dot{q}_w D_i}{\lambda_b Re_b^{1.625} Pr_b}\right)\left(\frac{\mu_{ave}}{\mu_b}\right)\left(\frac{\rho_{ave}}{\rho_b}\right)^{-0.5}, \tag{17}$$

states that when the value of ψ is lower than 0.385, the heat transfer impairment due to thermal acceleration can be neglected. For heat transfer studies of $scCO_2$ in either vertical or horizontal flow configurations, numerous authors [23,46,56] employed the dimensionless thermal acceleration parameter K_v proposed by McEligot et al. [57], which is defined as:

$$K_v = \frac{4\dot{q}_w D_i \beta_b}{Re_b^2 c_{p,b} \mu_b}. \tag{18}$$

For values of $K_v < 3 \bullet 10^{-6}$ the flow remains turbulent and the effect of flow *re-laminarization* can be ignored. Theologou et al. [26] used the criterion of Petukhov et al. [58], which predicts the heat transfer deterioration using the coefficients of acceleration resistance, ξ_{ac}, and friction resistance, ξ_{Pe}, given in Eqs. (19) and (20).

$$\xi_{ac} = 8q_b^+ \tag{19}$$

$$\xi_{Pe} = \left(\frac{\rho_w}{\rho_b}\right)^{0.4}\left[1.8\log\left(\frac{Re_b}{8}\right)\right]^2 \tag{20}$$

In Eq. (19), the dimensionless heat flux is expressed as $q_b^+ = \left(\beta_b \dot{q}_w\right)/\left(c_{p,b} G\right)$. Thus, when the ratio ξ_{ac}/ξ_{Pe} is lower than 1–1.3 the influence of flow acceleration on heat transfer is negligible.

Fig. B1 of the supplementary materials represents the thermal acceleration criterions of (a) Jackson, (b) McEligot and (c) Pethukov, plotted on a logarithmic scale as a function of distance from the heating onset for the 560 data points. According to the criterions, all experimental points lie below the respective threshold values. This result indicates that the heat transfer impairment due to thermal expansion-induced boundary layer *re-laminarization* can be considered negligible for the design of MSTE units in the NET Power cycle applications.

4. Development of a new heat transfer model based on deep learning

Numerous empirical correlations for the prediction of heat transfer coefficients for supercritical fluid flows have been developed. A complete survey of them, with their application ranges, are available in [20,22]. Most of the correlations were derived for $scCO_2$ or scH_2O through large-diameter vertical tubes. Regarding $scCO_2$ through horizontal tubes, the number of correlations available is significantly smaller, which is explained by the reduced amount of experimental data. This data gap is further intensified when considering microtubes with inner diameters of <1 mm. Table 2 lists the most widely employed heat transfer correlations in literature for $scCO_2$ through horizontal flow channels. Although some of them were derived for vertical flow orientation, they have proven to yield acceptable results for the horizontal configuration. These correlations are founded on the well-known constant-property turbulent flow Dittus-Boelter correlation [59],

$$Nu_b = 0.023 Re_b^{0.8} Pr_b^{0.4}, \tag{21}$$

and incorporate terms of property ratios to account for the large variation of fluid properties at bulk and wall temperatures.

The correlations of Liao et al. [27] and Wang et al. [37] were developed for microtubes. They include the Richarson number, *Ri*, to account for the heat transfer by buoyancy-induced natural convection. The Bishop correlation [60] demonstrated to predict heat transfer coefficients for $scCO_2$ in large diameter horizontal tubes with acceptable accuracy [26], despite it was fitted to experiments with upward flowing scH_2O. Moreover, the Bishop correlation considers the thermal inflow length as parameter. The correlations of Swenson et al. [61] and Preda et al. [62] were evaluated by Kim et al. for horizontal flows. In addition to the aforementioned heat transfer models, the Gnielinski correlation [63] for constant property turbulent flows at subcritical conditions, defined in Eq. (22), is commonly employed.

$$Nu = \frac{(f/8)(Re_b - 1000)Pr_b}{1 + 12.7(f/8)^{0.5}\left(Pr_b^{2/3} - 1\right)}\left[1 + \left(\frac{D_i}{x}\right)^{2/3}\right], \tag{22}$$

$$\text{with} f = \left(1.82\log_{10} Re_b - 1.64\right)^{-2}.$$

Predictions of these correlations are compared against the experimental data derived in this study using the mean average percentage error (MAPE), defined as follows:

$$\text{MAPE}\ (\%) = \frac{100}{N}\sum_{i=1}^{N}\left|\frac{\alpha_{\text{calc,i}} - \alpha_{\text{exp,i}}}{\alpha_{\text{exp,i}}}\right|, \tag{23}$$

where N is the number of experimental data points ($N = 560$). Comparison between the experimental and calculated Nusselt numbers from the correlations of Table 2, including the Gnielinski correlation, are depicted in Fig. 12. To quantitatively compare the performance of the correlations, the MAPE for all data points, as well as the percentage of predicted data within a range of 30 %, 40 % and 60 %, are shown in Table 3.

It can be found in Fig. 12 that the correlations overestimate the Nusselt numbers. The correlations of Liao et al. and Gnielinski reported the highest MAPE values; 164.49 % and 148.34 %, respectively. The correlation of Preda et al. proved to be the most accurate, with a MAPE of 66.53 %, followed by the correlation of Swenson et al., with a MAPE of 76.82 %. The overestimations can be explained by different reasons

Table 2
Heat transfer correlations for $scCO_2$ and scH_2O under heating conditions in horizontal and vertical flow configurations.

Authors	Correlation	Fluid and flow orientation	Application ranges
Liao et al. [27]	$Nu = 0.124Re_b^{0.8}Pr_b^{0.4}(Ri_b)^{0.203}\left(\frac{\rho_w}{\rho_b}\right)^{0.842}\left(\frac{\overline{c_p}}{c_{p,f}}\right)^{0.384}$ $Gr = \frac{(\rho_b-\rho_w)\rho_b g D_i^3}{\mu_b^2}$, $\overline{c_p} = \frac{h_w-h_b}{T_w-T_b}$	$ScCO_2$, horizontal	D_i = 0.7–2.16 mm p = 74–120 bar T_b = 20–110 °C $\dot{m}$ = 0.02–0.2 kg s^{-1} $Ri = 10^{-5}$-10^{-2}
Wang et al. [37]	$Nu = 0.225Re_f^{0.423}Pr_f^{0.229}(Ri_f)^{-0.156}(T^+)^{0.055}\left(\frac{\overline{c_p}}{c_{p,f}}\right)^{0.401}$ $T^+ = \frac{T_{pc}-T_{f,in}}{T_{f,out}-T_{f,in}}$, $\overline{c_p} = \frac{h_w-h_f}{T_w-T_f}$	$ScCO_2$, horizontal	D_i = 0.5–1.0 mm p = 76.6–90.0 bar T_{in} = 30.8–37.3 °C G = 672–4810 kg m^{-2} s^{-1} $\dot{q}_w$ = 70.7–344.2 kW m^{-2}
Bishop [60]	$Nu = 0.0069Re_b^{0.9}\overline{Pr}_b^{0.66}\left(\frac{\rho_w}{\rho_b}\right)^{0.43}\left(1+2.4\frac{D_i}{x}\right)\overline{Pr}_b = \frac{\overline{c}_p\mu_b}{\lambda_b}, \overline{c}_p = \frac{h_w-h_b}{T_w-T_b}$	ScH_2O, vertical (Upward)	p = 228–276 bar T_b = 282–527 °C G = 651-3662kg m^{-2} s^{-1} $\dot{q}_w$ = 0.31–3.46 MW m^{-2}
Swenson et al. [61]	$Nu = 0.00459Re_w^{0.923}\overline{Pr}_w^{0.613}\left(\frac{\rho_w}{\rho_b}\right)^{0.231}$	ScH_2O, vertical (upward)	D_i = 9.42 mm p = 227.5–413.7 bar T_b = 75–576 °C G = 543-2150kg m^{-2} s^{-1} $\dot{q}_w$ = 0.2–1.82 MW m^{-2}
Preda et al. [62]	$Nu = 0.0015Re_w^{1.03}\overline{Pr}_w^{0.76}\left(\frac{\rho_w}{\rho_b}\right)^{0.46}\left(\frac{\mu_w}{\mu_b}\right)^{0.53}\left(\frac{\lambda_w}{\lambda_b}\right)^{-0.43}$	$ScCO_2$, vertical (upward)	p = 81.2 bar T_b = 25–125 °C G = 430-1200kg m^{-2} s^{-1} $\dot{q}_w$ = 49–135 MW m^{-2}

depending on the operating pressure.

Near the critical point (i.e., 10 MPa), the correlations for supercritical fluid flows in Table 2 were fitted for a narrow application range. When applied beyond that range, their predictive accuracy deteriorates. Kim et al. [36] and Theologou et al. [26] also reported significant overpredictions of the Nusselt numbers when challenging various correlations against their experimental data. This suggests that the strength of buoyancy forces is not properly captured by the correlations. In particular, Theologou et al. tested the correlations of Gnielinski, Bishop et al., Liao et al., and Lei et al. [64], finding MAPE values of 308 %, 89 %, 248 %, and 213 %, respectively.

As the test pressure increases (between 15 and 30 MPa), the fluid viscosity rises, leading to a significant reduction in Reynolds numbers, as shown in Table A1. In fact, 56 % of the heat transfer coefficients were acquired at Reynolds numbers below 10^4. Under the smooth conditions of the experimental tests, this implies that certain flow regions likely remain in the transitional regime, where viscosity limits efficient transverse fluid mixing. This is manifested by the progressive separation between wall and bulk fluid temperature profiles shown, for example, in Fig. 10(i). In contrast, the conventional Gnielinski correlation, valid for Reynolds numbers between 10^4 and 10^6 [63], assumes fully developed turbulence. In this flow regime, heat transfer rates are considerably higher than in transitional flow, which explains the overprediction of the Nusselt numbers observed in Fig. 12. Furthermore, it is noticeable from Fig. 12 that the higher the Nusselt number (i.e., higher Reynolds), the more accurate the predictions are, reinforcing this physical interpretation. Additionally, the flow laminarization effect is accentuated at high pressures due to the reduced axial flow acceleration, which increases the residence time. This favors the accumulation of low-momentum fluid on the top wall, delaying the flow development towards the turbulent regime.

To propose a novel feasible heat transfer model, an artificial deep neural network (DNN), with the structure presented in Fig. 13, was developed for the 560 experimental Nusselt number data points ($Nu_{DNN} = DNN(\boldsymbol{x})$) [47]. In this work, deep learning techniques offer an efficient strategy to develop predictive models capable of coherently integrating all the highly non-linear heat transfer effects identified in the experimental results. The DNN includes four layers: an input layer; two hidden layers with 15 and 10 units, respectively; and an output layer.

The inputs to the model are expressed in Eq. (24) by the input vector $\boldsymbol{x}$.

$$Nu_{b,DNN} = DNN(\boldsymbol{x}), \text{with} \boldsymbol{x} = \left\{Re_b, Pr_b, \frac{\rho_w}{\rho_b}, \frac{\mu_w}{\mu_b}, \frac{\lambda_w}{\lambda_b}, \frac{\overline{c_p}}{c_{p,f}}, \frac{x}{D_i}, \frac{p_{in}}{p_{cr}}\right\} \tag{24}$$

The property ratios account for the variation of the fluid properties between the near-wall region and the bulk. The x/D_i ratio allows modeling the thermal inflow effects. The heat transfer performance of $scCO_2$ is strongly affected by pressure. Although the influence of pressure is embedded in the fluid properties, a significant improvement in the predictive capability of the model was found when the reduced pressure (p_{in}/p_{cr}) was included as an input. p_{cr} denotes the critical pressure of CO_2 (~73.8 bar). The hyperbolic sigmoid function (tansig) [65] was used as the activation function for the hidden layers. Then, the output of the j th hidden unit (HU), of the first hidden layer, can be computed as follows:

$$HU_{1j} = \text{tansig}\left(\sum_{i=1}^{N_{in}} w_{1ji}x_i + b_{1j}\right), \tag{25}$$

where i is the i th input, w are the synaptic weights, b the bias and N_{in} the total number of inputs. In general, the output of the j th HU of the k th layer is calculated according to Eq. (26).

$$HU_{kj} = \text{tansig}\left(\sum_{i=1}^{N_{HU_{k-1}}} w_{kji}HU_{k-1,i} + b_{kj}\right). \tag{26}$$

N_{HUk} denotes the total number of HU s in the k th layer. Then, the output results:

$$DNN(\boldsymbol{x}) = \sum_{i=1}^{N_{HU_{M-1}}} w_{o,i}HU_{M-1,i} + b_o, \tag{27}$$

where M is the number of layers. The DNN model, together with the experimental Nusselt numbers, were entered in Matlab R2022b. The weights and bias were trained using the Levenberg-Marquardt algorithm to minimize the mean squared error. The experimental data were partitioned into training, validation, and test sets. This division strategy was implemented to reduce the risk of overfitting and to enhance the generalization capability of the network. The dataset were divided into 70 % for training, 15 % for validation, and 15 % for test. This partition was found after evaluating three random configurations using 60 %, 70 %, and 80 % of the data assigned for training. For the three divisions, the

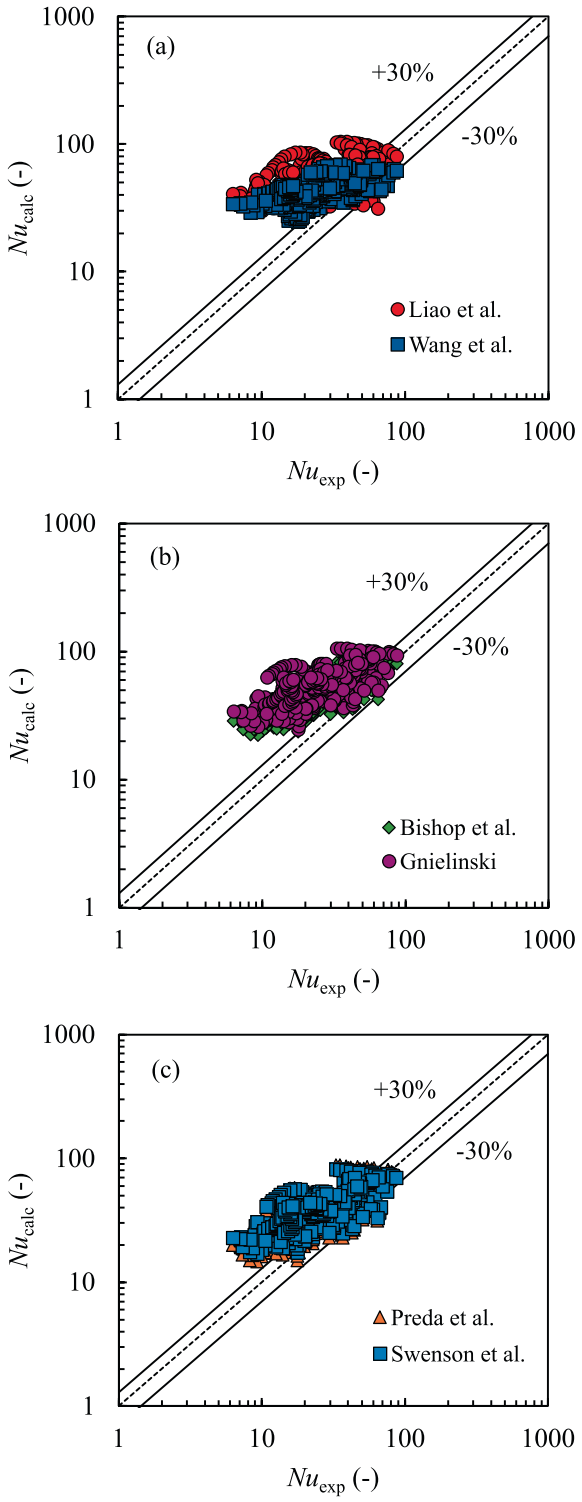

Fig. 12. Comparison of experimental and calculated data in terms of the Nusselt number. The considered correlations were: (a) Liao et al. [27] and Wang et al. [37], (b) Bishop et al. [60] and Gnielinski [63], (c) Preda et al. [62] and Swenson et al. [61]. Correlations overestimate the Nusselt numbers mainly due to the low experimental Reynolds numbers.

results reported minimal variations in the mean squared error and generalization capability due to the uniformity of the dataset within the experimental domain. The 70/15/15 division provided best overall coefficient of determination ($R^2 = 0.99681$) without overfitting the model. The resulting weights and bias are given in Appendix C of the supplementary materials, for a miniature tube of $D_i = 0.88$ mm in the application range of $10 \leq p_{in} \leq 30$ MPa, $4099.9 \leq Re_b \leq 23847.4$, $19.8 \leq T_b \leq 101.8$ °C, $447.4 \leq G \leq 1355.2$ kg m^{-2} s^{-1}, and $8.3 \leq \dot{q}_w \leq 21.3$ kW m^{-2}.

Table 3
Comparison of the prediction accuracy among the evaluated heat transfer models. The DNN-based heat transfer model, with a MAPE of 6.74 %, significantly improves prediction accuracy compared to the correlation of Preda et al.

Correlations	MAPE (%)	Percentage of data predicted within		
		30 %	40 %	60 %
Liao et al. [27]	164.49	8.59	12.11	24.89
Wang et al. [37]	114.01	20.70	28.19	40.31
Bishop et al. [60]	113.51	11.01	16.08	30.18
Gnielinski [63]	148.34	8.15	9.91	20.48
Preda et al. [62]	66.53	31.72	41.19	57.27
Swenson et al. [61]	76.82	28.41	33.92	49.56
DNN (present work)	6.74	98.68	99.78	100.00

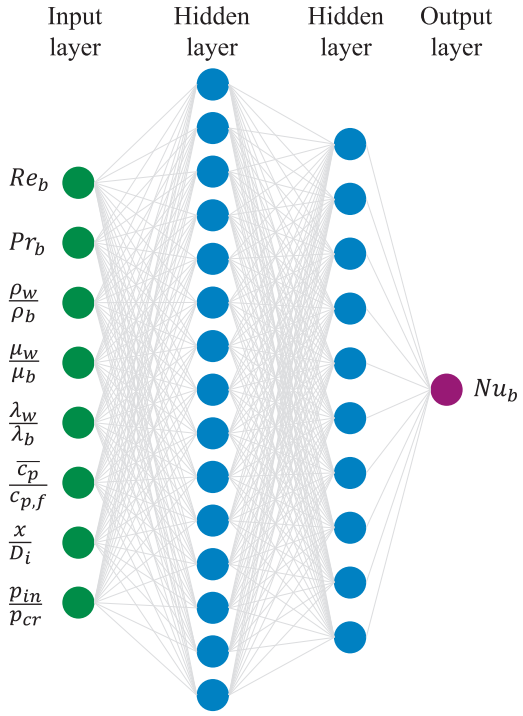

Fig. 13. Structure of the artificial deep neural network-based heat transfer model. The DNN consists of four layers: an input layer, two hidden layers, and an output layer.

The comparison between the experimental and the DNN predicted Nusselt number values are illustrated in Fig. 14. It can be deduced that the DNN-based heat transfer model improves the predictions with respect to the existing correlations. As can be seen in Table 3, the DNN captures the experimental data with a MAPE of 4.32 %, with 100 % of the data satisfying a relative deviation of less than 30 %. These results indicate that the new heat transfer model can be used for MSTE design purposes for the low-temperature exchange section of the NET Power cycle within the specified applicability range. However, beyond this range, the limited availability of experimental data on $scCO_2$ heat transfer in miniature tubes under cycle-relevant conditions restricts external validation and a full assessment of the predictive capability of the DNN model.

5. Conclusions

This paper experimentally investigated heat transfer in supercritical

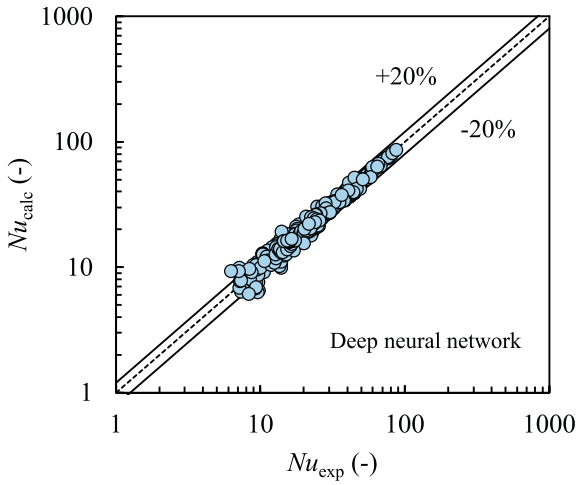

Fig. 14. Comparison of experimental and calculated data in terms of the Nusselt number for the artificial deep neural network heat transfer model developed in this work. 94.49% of the data satisfies a relative deviation of <20 %.

CO_2 up to 30 MPa in a horizontal microtube of 1700 mm length and 0.88 mm inner diameter, uniformly heated, reproducing the conditions of a micro shell-and-tube exchanger (MSTE) for the NET Power cycle. Unlike previous studies, which focused on near-critical pressures and large-diameter tubes, the main novelty of this research is the extension of the experimental pressure range up to 30 MPa, representative of real MSTE operating conditions. This enabled the identification of heat transfer phenomena that had not been previously reported or were insufficiently explored in the literature. The results provide a new set of local heat transfer data applicable to the design of MSTEs for the NET Power cycle, supporting the transition from the established printed circuit heat exchangers to micro shell-and-tube configurations.

A parametric study was conducted to analyze the influence of mass flux, heat flux, inlet temperature, buoyancy and flow acceleration on heat transfer at five pressure levels between 10 and 30 MPa. Heat transfer coefficients increased with mass flux for all tested pressures. At 10 MPa, the coefficient exhibited a pronounced peak near the pseudo-critical point, rising from 1.35 to 5.38 kW m^{-2} K^{-1} as mass flux increased from 447.4 to 604.9 kg m^{-2} s^{-1}. Following this peak, a deterioration-recovery pattern was identified, forming a "valley region" associated with buoyancy and axial flow acceleration effects. This finding confirms a phenomenon previously reported only once and provides a clear physical explanation of the recovery section, demonstrating its strong dependence on mass flux. Between 15 and 30 MPa, the coefficients stabilized, exhibiting a more uniform trend in the fully developed thermal region.

Sensitivity analysis revealed that the local response of the heat transfer coefficient to heat flux and inlet temperature varies significantly with pressure. At 10 MPa, the maximum value increased from 1.35 to 2.0 kW m^{-2} K^{-1} when the heat flux decreased from 14.8 to 9.5 kW m^{-2}, whereas at 15–30 MPa the opposite behavior was found, with improved heat transfer at higher thermal loads. These trends, quantified locally for the first time in miniature tubes, constitute a novel contribution to the thermal–hydraulic design of MSTEs under both low- and high-load cycle conditions. At 25 and 30 MPa, a longer thermal inflow length was observed, attributable to the increased fluid viscosity. Increasing inlet temperature enhanced heat transfer in the thermal entrance region at all pressures, improving the MSTE effectiveness on the cold-side under high-load conditions. The peak of the heat transfer coefficient decreased with higher inlet temperatures, although the fluid temperature at which the peak occurs remained unchanged. At higher pressures, the coefficients converged to similar values in the fully developed region regardless of inlet temperature.

Buoyancy and thermal stratification effects were critical at low pressures. At 10 MPa, buoyancy was significant and decreased with increasing pressure. Moreover, for experimental points with high $\dot{q}_w/G$ ratios, mixed convection was observed in all cases. This finding becomes critical regarding the design of MSTEs. According to the Jackson criterion, this work reported the axial distance at which buoyancy becomes relevant as a function of pressure. Therefore, these results represent the first quantitative characterization of the onset of buoyancy and stratification effects in microtubes, providing critical insights for MSTE durability and reliability. Flow acceleration-induced deterioration was negligible, revealing that re-laminarization has a limited impact within the operational range of the MSTE.

Finally, a predictive heat transfer model, based on a deep neural network (DNN), was developed using the experimental dataset. Unlike traditional correlations, deep learning allowed coherent integration of all experimentally observed effects on heat transfer mechanisms into a unified predictive framework. The DNN model captures the experimental data with an average deviation of 6.74 %, demonstrating its accuracy and direct applicability for MSTE design for the NET Power cycle.

Future research could focus on:

- Extending the ranges of the experimental variables in order to investigate a wider thermodynamic domain of the NET Power cycle, thereby improving the generalization and predictive accuracy of the developed DNN-based heat transfer model.
- Conducting a comprehensive investigation of pressure drop in $scCO_2$ microflows under the relevant operating conditions of the NET Power cycle, as this parameter is pivotal in the design and optimization of MSTE units.
- Testing in a scaled experimental version of an MSTE unit incorporating multiple parallel flow channels to study the influence of inter-channel thermal–hydraulic interactions on heat transfer and pressure drop characteristics. The present study was limited to a single microchannel configuration, designed to derive local heat transfer coefficients to: (i) experimentally assess the fundamental heat transfer mechanisms in $scCO_2$ microflows, and (ii) propose a reliable heat transfer model for future system-scale applications.

Declaration of competing interest

The authors declare that they have no known competing financial interests or personal relationships that could have appeared to influence the work reported in this paper.

Acknowledgements

This research work was funded by the University of Valladolid, Spain, through the research project 061/2209311. Authors would like to acknowledge the entities Engie and TES-H2, and the research groups in high pressure technologies (PressTech) and in thermal engines and renewable energies (MyER), of the University of Valladolid, for the technical contribution during the realization of this research work.

Appendix A. Supplementary data

Supplementary data to this article can be found online at https://doi.org/10.1016/j.applthermaleng.2025.129206.

Data availability

Data will be made available on request.

References

[1] I. Velázquez, F. Demeyer, M. Reyes, Investigation of the impact of the thermodynamic property method on the performance, preliminary component sizing and maximum efficiency configuration of the NET power cycle, Appl. Therm. Eng. (2025) 126491, https://doi.org/10.1016/j.applthermaleng.2025.126491.

[2] L. Mancuso, N. Ferrar, P. Chiesa, E. Martelli, M. Romano, Oxy-Combustion Turbine Power Plants, 2015. www.ieaghg.org. (Accessed July 9, 2025).

[3] D.Y.C. Leung, G. Caramanna, M.M. Maroto-Valer, An overview of current status of carbon dioxide capture and storage technologies, Renew. Sustain. Energy Rev. 39 (2014) 426–443, https://doi.org/10.1016/J.RSER.2014.07.093.

[4] F. Climent Barba, G. Martínez-Denegri Sánchez, B. Soler Seguí, H. Gohari Darabkhani, E.J. Anthony, A technical evaluation, performance analysis and risk assessment of multiple novel oxy-turbine power cycles with complete CO_2 capture, J. Clean. Prod. 133 (2016) 971–985, https://doi.org/10.1016/j.jclepro.2016.05.189.

[5] W. Chan, T. Morosuk, X. Li, H. Li, Allam cycle: review of research and development, Energy Convers. Manag. 294 (2023) 117607, https://doi.org/10.1016/j.enconman.2023.117607.

[6] R. Scaccabarozzi, M. Gatti, E. Martelli, Thermodynamic analysis and numerical optimization of the NET Power oxy-combustion cycle, Appl. Energy 178 (2016) 505–526, https://doi.org/10.1016/j.apenergy.2016.06.060.

[7] R. Allam, S. Martin, B. Forrest, J. Fetvedt, X. Lu, D. Freed, G.W. Brown, T. Sasaki, M. Itoh, J. Manning, Demonstration of the allam cycle: an update on the development status of a high efficiency supercritical carbon dioxide power process employing full carbon capture, in: Energy Procedia, Elsevier Ltd, 2017, pp. 5948–5966, https://doi.org/10.1016/j.egypro.2017.03.1731.

[8] J.S. Kwon, S. Son, J.Y. Heo, J.I. Lee, Compact heat exchangers for supercritical CO_2 power cycle application, Energy Convers. Manag. 209 (2020) 112666, https://doi.org/10.1016/j.enconman.2020.112666.

[9] K. Brun, P. Friedman, R. Dennis. Fundamentals and Applications of Supercritical Carbon Dioxide (sCO_2) Based Power Cycles, Woodhead Publishing Series in Energy, 2017.

[10] M. Bernades, F. Capuano, L. Jofre, Microconfined high-pressure transcritical fluid turbulence, Phys. Fluids 35 (2023), https://doi.org/10.1063/5.0135388.

[11] A. Meshram, A.K. Jaiswal, S.D. Khivsara, J.D. Ortega, C. Ho, R. Bapat, P. Dutta, Modeling and analysis of a printed circuit heat exchanger for supercritical CO_2 power cycle applications, Appl. Therm. Eng. 109 (2016) 861–870, https://doi.org/10.1016/j.applthermaleng.2016.05.033.

[12] N. Kazakov. Diffusion Bonding of Materials, Elsevier, 2013.

[13] L. Chordia, M.A. Portnoff, E. Green, High Temperature Heat Exchanger Design and Fabrication for Systems with Large Pressure Differentials, Pittsburgh, PA, and Morgantown, WV (United States), 2017. doi: 10.2172/1349235.

[14] Y. Jiang, E. Liese, S.E. Zitney, D. Bhattacharyya, Optimal design of microtube recuperators for an indirect supercritical carbon dioxide recompression closed Brayton cycle, Appl. Energy 216 (2018) 634–648, https://doi.org/10.1016/j.apenergy.2018.02.082.

[15] Y. Jiang, E.A. Liese, S.E. Zitney, D. Bhattacharyya, Dynamic modeling of microtube recuperators in an indirect supercritical carbon dioxide recompression closed Brayton power cycle, in: The 6Th International Supercritical CO_2 Power Cycles Symposium, 2018.

[16] Y.H. Fan, G.H. Tang, X.L. Li, D.L. Yang, General and unique issues at multiple scales for supercritical carbon dioxide power system: a review on recent advances, Energy Convers. Manag. 268 (2022) 115993, https://doi.org/10.1016/j.enconman.2022.115993.

[17] V. Firouzdor, K. Sridharan, G. Cao, M. Anderson, T.R. Allen, Corrosion of a stainless steel and nickel-based alloys in high temperature supercritical carbon dioxide environment, Corros. Sci. 69 (2013) 281–291, https://doi.org/10.1016/j.corsci.2012.11.041.

[18] I. Velázquez, F. Demeyer, M. Reyes, Optimization and performance evaluation of equations of state for supercritical CO_2-rich mixtures for application in the NET Power cycle, J. Supercrit. Fluids (2025) 106693, https://doi.org/10.1016/j.supflu.2025.106693.

[19] X. Cheng, X.J. Liu, Research challenges of heat transfer to supercritical fluids, J. Nucl. Eng. Radiat. Sci. 4 (2018), https://doi.org/10.1115/1.4037117.

[20] L.F. Cabeza, A. de Gracia, A.I. Fernández, M.M. Farid, Supercritical CO_2 as heat transfer fluid: a review, Appl. Therm. Eng. 125 (2017) 799–810, https://doi.org/10.1016/j.applthermaleng.2017.07.049.

[21] X.R. Zhang, H. Yamaguchi, Forced convection heat transfer of supercritical CO_2 in a horizontal circular tube, J. Supercrit. Fluids 41 (2007) 412–420, https://doi.org/10.1016/j.supflu.2006.11.003.

[22] D. Wu, M. Wei, R. Tian, S. Zheng, J. He, A review of flow and heat transfer characteristics of supercritical carbon dioxide under cooling conditions in energy and power systems, Energies 15 (2022) 8785, https://doi.org/10.3390/en15238785.

[23] M. Xiang, J. Guo, X. Huai, X. Cui, Thermal analysis of supercritical pressure CO_2 in horizontal tubes under cooling condition, J. Supercrit. Fluids 130 (2017) 389–398, https://doi.org/10.1016/j.supflu.2017.04.009.

[24] H. Zhang, J. Guo, X. Cui, X. Huai, Heat transfer performance of supercritical pressure CO_2 in a non-uniformly heated horizontal tube, Int. J. Heat Mass Transf. 155 (2020) 119748, https://doi.org/10.1016/j.ijheatmasstransfer.2020.119748.

[25] G.A. Adebiyi, W.B. Hall, Experimental Investigation of heat transfer to supercritical pressure carbon dioxide in a horizontal pipe, Int. J. Heat Mass Transfer 19 (1975), https://doi.org/10.1016/0017-9310(76)90123-X-.

[26] K. Theologou, R. Mertz, E. Laurien, J. Starflinger, Experimental investigations on heat transfer of CO_2 under supercritical pressure in heated horizontal pipes, Energy 254 (2022) 124171, https://doi.org/10.1016/j.energy.2022.124171.

[27] S.M. Liao, T.S. Zhao, An experimental investigation of convection heat transfer to supercritical carbon dioxide in miniature tubes, Int. J. Heat Mass Transf. (2002) 5025–5034, https://doi.org/10.1016/S0017-9310(02)00206-5.

[28] S.H. Yoon, J.H. Kim, Y.W. Hwang, M.S. Kim, K. Min, Y. Kim, Heat transfer and pressure drop characteristics during the in-tube cooling process of carbon dioxide in the supercritical region, Int. J. Refrig. 26 (2003) 857–864, https://doi.org/10.1016/S0140-7007(03)00096-3.

[29] C. Dang, E. Hihara, In-tube cooling heat transfer of supercritical carbon dioxide. Part 1. Experimental measurement, Int. J. Refrig. 27 (2004) 736–747, https://doi.org/10.1016/j.ijrefrig.2004.04.018.

[30] X.L. Huai, S. Koyama, T.S. Zhao, An experimental study of flow and heat transfer of supercritical carbon dioxide in multi-port mini channels under cooling conditions, Chem. Eng. Sci. 60 (2005) 3337–3345, https://doi.org/10.1016/j.ces.2005.02.039.

[31] C.-H. Son, S.-J. Park, An experimental study on heat transfer and pressure drop characteristics of carbon dioxide during gas cooling process in a horizontal tube, Int. J. Refrig. 29 (2006) 539–546, https://doi.org/10.1016/j.ijrefrig.2005.10.010.

[32] H.-K. Oh, C.-H. Son, New correlation to predict the heat transfer coefficient in-tube cooling of supercritical CO_2 in horizontal macro-tubes, Exp. Therm Fluid Sci. 34 (2010) 1230–1241, https://doi.org/10.1016/j.expthermflusci.2010.05.002.

[33] S.S. Pitla, E.A. Groll, S. Ramadhyani, Convective heat transfer from in-tube cooling of turbulent supercritical carbon dioxide: Part 2—Experimental data and numerical predictions, HVAC&R Res. 7 (2001) 367–382, https://doi.org/10.1080/10789669.2001.10391281.

[34] Z.-B. Liu, Y.-L. He, Y.-F. Yang, J.-Y. Fei, Experimental study on heat transfer and pressure drop of supercritical CO_2 cooled in a large tube, Appl. Therm. Eng. 70 (2014) 307–315, https://doi.org/10.1016/j.applthermaleng.2014.05.024.

[35] S.A. Jajja, K.R. Zada, B.M. Fronk, Experimental investigation of supercritical carbon dioxide in horizontal microchannels with non-uniform heat flux boundary conditions, Int. J. Heat Mass Transf. 130 (2019) 304–319, https://doi.org/10.1016/j.ijheatmasstransfer.2018.10.027.

[36] T.H. Kim, J.G. Kwon, J.H. Park, H.S. Park, M.H. Kim, Heat transfer model for horizontal flows of CO_2 at supercritical pressures in terms of mixed convection, Int. J. Heat Mass Transf. 131 (2019) 1117–1128, https://doi.org/10.1016/j.ijheatmasstransfer.2018.11.075.

[37] L. Wang, Y.C. Pan, J. Der Lee, Y. Wang, B.-R. Fu, C. Pan, Experimental investigation in the local heat transfer of supercritical carbon dioxide in the uniformly heated horizontal miniature tubes, Int. J. Heat Mass Transf. 159 (2020) 120136, https://doi.org/10.1016/j.ijheatmasstransfer.2020.120136.

[38] E. Öztabak, O. Gökkaya, H. Ahn, Heat transfer characteristics of horizontal supercritical CO_2 flow through a microtube at low Reynolds numbers and its comparison with vertical flows, Exp. Therm Fluid Sci. 147 (2023) 110957, https://doi.org/10.1016/j.expthermflusci.2023.110957.

[39] J. Xie, D. Liu, H. Yan, G. Xie, S.K.S. Boetcher, A review of heat transfer deterioration of supercritical carbon dioxide flowing in vertical tubes: Heat transfer behaviors, identification methods, critical heat fluxes, and heat transfer correlations, Int. J. Heat Mass Transf. 149 (2020) 119233, https://doi.org/10.1016/j.ijheatmasstransfer.2019.119233.

[40] National Instruments Corp., LabVIEW 2024 Q1, 2024.

[41] E.W. Lemmon, I.H. Bell, M.L. Huber, M.O. McLinden, NIST Standard Reference Database 23: Reference Fluid Thermodynamic and Transport Properties-REFPROP, Version 10.0, National Institute of Standards and Technology, 2018.

[42] S.J. Kline, F.A. McClintock, Describing uncertainties in single-sample experiments, Mechanical Engineering (1953).

[43] Inc. Statgraphics Technologies, Statgraphics Centurion 19, 2024.

[44] S.A. Zaryab, R. Scaccabarozzi, E. Martelli, Advanced part-load control strategies for the Allam cycle, Appl. Therm. Eng. 168 (2020), https://doi.org/10.1016/j.applthermaleng.2019.114822.

[45] J.M. Coulson, J.F. Richardson. Chemical engineering, 6th ed., Elsevier, 1993 https://doi.org/10.1016/C2009-0-11215-1.

[46] D.E. Kim, M.-H. Kim, Experimental investigation of heat transfer in vertical upward and downward supercritical CO_2 flow in a circular tube, Int. J. Heat Fluid Flow 32 (2011) 176–191, https://doi.org/10.1016/j.ijheatfluidflow.2010.09.001.

[47] X. Lei, J. Zhang, L. Gou, Q. Zhang, H. Li, Experimental study on convection heat transfer of supercritical CO_2 in small upward channels, Energy 176 (2019) 119–130, https://doi.org/10.1016/j.energy.2019.03.109.

[48] B. Zhu, J. Xu, X. Wu, J. Xie, M. Li, Supercritical "boiling" number, a new parameter to distinguish two regimes of carbon dioxide heat transfer in tubes, Int. J. Therm. Sci. 136 (2019) 254–266, https://doi.org/10.1016/j.ijthermalsci.2018.10.032.

[49] J. Wang, Z. Guan, H. Gurgenci, K. Hooman, A. Veeraragavan, X. Kang, Computational investigations of heat transfer to supercritical CO_2 in a large horizontal tube, Energy Convers. Manag. 157 (2018) 536–548, https://doi.org/10.1016/j.enconman.2017.12.046.

[50] Y.A. Cengel, A.J. Ghajar. Heat and Mass Transfer: Fundamentals and Applications, fourth ed., McGraw-Hill Education, 2011.

[51] X. Chu, E. Laurien, Flow stratification of supercritical CO_2 in a heated horizontal pipe, J. Supercrit. Fluids 116 (2016) 172–189, https://doi.org/10.1016/j.supflu.2016.05.003.

[52] Y. Zhang, M. Peng, G. Xia, T. Cong, Numerical investigation on local heat transfer characteristics of S-CO_2 in horizontal semicircular microtube, Appl. Therm. Eng. 154 (2019) 380–392, https://doi.org/10.1016/j.applthermaleng.2019.03.082.

[53] B.S. Petukhov, A.F. Poliakov, B.E. Launder, A.F. Poleiakov, Heat transfer in turbulent mixed convection, Hemisphere Pub. Corp. 1988. https://inis.iaea.org/search/search.aspx?orig_q=RN:19092970 (accessed December 13, 2024).
[54] K. Tanimizu, R. Sadr, Experimental investigation of buoyancy effects on convection heat transfer of supercritical CO_2 flow in a horizontal tube, Heat Mass Transf. 52 (2016) 713–726, https://doi.org/10.1007/s00231-015-1580-9.
[55] J.D. Jackson, Models of heat transfer to fluids at supercritical pressure with influences of buoyancy and acceleration, Appl. Therm. Eng. 124 (2017) 1481–1491, https://doi.org/10.1016/j.applthermaleng.2017.03.146.
[56] P.-X. Jiang, B. Liu, C.-R. Zhao, F. Luo, Convection heat transfer of supercritical pressure carbon dioxide in a vertical micro tube from transition to turbulent flow regime, Int. J. Heat Mass Transf. 56 (2013) 741–749, https://doi.org/10.1016/j.ijheatmasstransfer.2012.08.038.
[57] D.M. McEligot, C.W. Coon, H.C. Perkins, Relaminarization in tubes, Int. J. Heat Mass Transf. 13 (1970) 431–433, https://doi.org/10.1016/0017-9310(70)90118-3.
[58] B. Petukhov, B. Kurganov, B. Ankudinov, Heat transfer and flow resistance in the turbulent pipe flow of a fluid with near-critical state parameters, Inst. High Temps. 21 (1983) 92–100.
[59] F. Dittus, L. Boelter, Heat transfer in automobile radiators of the tubular type, Int. Commun. Heat Mass Transf. 12 (1985) 3–22, https://doi.org/10.1016/0735-1933(85)90003-X.
[60] I.L. Pioro, H.F. Khartabil, R.B. Duffey, Heat transfer to supercritical fluids flowing in channels-empirical correlations (survey), Nucl. Eng. Des. 230 (2004) 69–91, https://doi.org/10.1016/j.nucengdes.2003.10.010.
[61] H.S. Swenson, J.R. Carver, C.R. Kakarala, Heat transfer to supercritical water in smooth-bore tubes, J. Heat Transf. 87 (1965) 477–483, https://doi.org/10.1115/1.3689139.
[62] T. Preda, E. Saltanov, I. Pioro, K.S. Gabriel, Development of a heat transfer correlation for supercritical CO_2 based on multiple data sets, in: Volume 5: Fusion Engineering; Student Paper Competition; Design Basis and Beyond Design Basis Events; Simple and Combined Cycles, ASME, 2012, pp. 211–217. doi: 10.1115/ICONE20-POWER2012-54516.
[63] Verein Deutscher Ingenieure, VDI Heat Atlas, Springer Berlin Heidelberg, 2010. doi: 10.1007/978-3-540-77877-6.
[64] X. Lei, H. Li, N. Dinh, W. Zhang, A study of heat transfer scaling of supercritical pressure water in horizontal tubes, Int. J. Heat Mass Transf. 114 (2017) 923–933, https://doi.org/10.1016/j.ijheatmasstransfer.2017.06.052.
[65] A. Menon, K. Mehrotra, C.K. Mohan, S. Ranka, Characterization of a class of sigmoid functions with applications to neural networks, Neural Netw. 9 (1996) 819–835, https://doi.org/10.1016/0893-6080(95)00107-7.